



LUND
UNIVERSITY

MASTER'S THESIS

Supersymmetric searches in the 2-electron channel

Author:
WONG Ming Liang

Supervisor:
Dr. Else LYTKEN

February 21, 2012

Abstract

The Standard Model (SM) has been very successfully used to explain many physical phenomena. However, the theory has several problems such as not being able to be unified with gravitation and the hierarchy problem. The cosmological mystery of dark matter also gives a hint that the Standard Model is not the full story and cannot explain all matter that exists in our universe. Supersymmetry (SUSY) is one of the extensions of the SM which could elegantly solve all the problems aforementioned. In this thesis, we attempt to look for $\tilde{\chi}_2^0$ from the mSUGRA and MSSM24 theoretical frameworks using the dielectron channel by studying the invariant dielectron mass and missing transverse energy. Another technique used as a comparison is the sliding q_T method which analyses the total momentum of the dielectrons. Data from the ATLAS detector using pp collisions at $\sqrt{s} = 7\text{TeV}$ with integrated luminosity of about 1.6 fb^{-1} is used. In addition to that, several improvements to the grid job submission mechanism is shown using Python multithreading to send multiple jobs to the grid cluster thus increasing efficiency in job submission and failure management.

Sammanfattning

Standard Modellen (SM) har framgångsrikt förklarat många fysikaliska fenomen. Teorin har emellertid flera problem, som exempelvis oförmågan att kunna förenas med gravitation och hierarkiproblemet. Det kosmologiska mysteriet med mörk materia ger också en vink om att Standard Modellen inte innehåller hela sanningen och inte kan förklara all materia som förekommer i vårt universum. Supersymmetri (SUSY) är en av utvidgningarna av SM som kan, på ett elegant sätt, lösa de nämnda problemen. I denna avhandling försöker vi med hjälp av de teoretiska ramverken mSUGRA och MSSM24, via dielektron kanalen hitta $\tilde{\chi}_2^0$ genom att studera den invarianta massan hos dielektronerna och saknad transvers energi. En annan teknik som används är den glidande q_T -metoden som analyserar dielektronernas totala rörelsemängd. Proton-proton data från ATLAS-detektorn vid $\sqrt{s} = 7$ TeV, med en integrerad luminositet på cirka 1.6 fb^{-1} , har använts. I avhandlingen diskuteras också flera förbättringar av hur man skickar iväg ett jobb till gridden, där man använder Python multithreading för att skicka multipla jobb till gridd-klustret och på så sätt öka effektiviteten för jobben och hanterandet av misslyckade jobb.

Contents

1	The Standard Model and Supersymmetry	1
1.1	The Standard Model	1
1.2	Standard model particles and forces	1
1.3	Limitations of the SM and Supersymmetry	5
1.4	Soft SUSY breaking	8
2	SUSY models	10
2.1	MSSM	10
2.1.1	Electroweak symmetry breaking	12
2.2	mSUGRA	14
2.3	MSSM24	17
3	LHC and the ATLAS Detector	21
3.1	The Inner Detector	26
3.2	Electromagnetic Calorimeter	26
3.3	Hadronic Calorimeter	27
3.4	Muon Spectrometer	28
3.5	Triggers	30
3.6	Supersymmetric event displays	33
4	Grid Computing	36
4.1	WLCG	36
4.2	NorduGrid and ARC	38
4.3	Multithreaded processing on LXPLUS	40
4.4	Multithreaded arclib job submission	42
4.5	Offline ROOT file operations	42
5	Analysis	45
5.1	Finding the $\tilde{\chi}_2^0$	45
5.2	Monte Carlo Samples	46
5.3	Electron Identification	51

5.4	Systematics, Energy rescaling and Pileup reweightings	56
5.5	Dielectron channel studies	57
5.6	Sliding q_T Ratio Method	64
6	Conclusion	77
	Nomenclature	78
	Appendices	79
A	SM D3PD	80

Chapter 1

The Standard Model and Supersymmetry

1.1 The Standard Model

The Standard Model (SM) of particle physics is a theory incorporating the electromagnetic, weak, and strong nuclear interactions, which mediate the dynamics of the known subatomic particles. Developed throughout the mid to late 20th century, the current formulation was finalized in the mid 1970s upon experimental confirmation of the existence of quarks. Since then, discoveries of the bottom quark (1977), the top quark (1995), W and Z bosons (1984), and the tau neutrino (2000) have given credence to the Standard Model. Because of its success in explaining a wide variety of experimental results, the Standard Model is sometimes regarded as a theory of almost everything.

1.2 Standard model particles and forces

Using the SM, we are able to describe fermions, gauge bosons, the Higgs boson, and their interactions. We currently have 12 fermions, left- and right-handed and their anti-fermion partners. They come in three generations. These fermions are further classified as leptons and quarks. (u, d, e^-, ν_e) belong to the first generation, (c, s, μ^-, ν_μ) belong to the second generation and (t, b, τ^-, ν_τ) belong to the third generation. The theory also predicts that there are three generations of fermions.

The idea of gauge invariance is central to the development of the SM. It stems from electrodynamics where a change of phase in the scalar(electric) potential, $\psi' \rightarrow \psi e^{-i\chi}$ does not modify the physics of the theory. Together

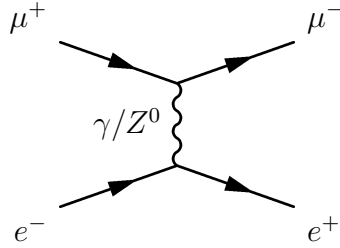


Figure 1.1: t-channel $e^+ e^-$ annihilation creating a muon-antimuon pair. This is an example of an interaction which can happen electromagnetically via photons or weakly via Z bosons.

with the vector potential, $A'_\mu \rightarrow A_\mu + \partial_\mu \chi$, they form the set of equations for local gauge transformation.

It is also important for the Lagrangian to be invariant under local gauge transformations. Therefore, the covariant derivative, $\mathcal{D}_\mu \equiv \partial_\mu - ieA_\mu$ instead of just ∂_μ is used for that purpose.

Since all charged particles interact electromagnetically, they have U(1) invariance¹ with the photon as the gauge boson required by the invariance of the theory. In addition to that, all known particles interact weakly and appear to have a SU(2)² invariance with the gauge fields, $W_i^\mu (i = 1, 2, 3)$ for gauge invariance. Left-handed quarks are also involved in the strong interaction, having SU(3) invariance with eight gluon fields.

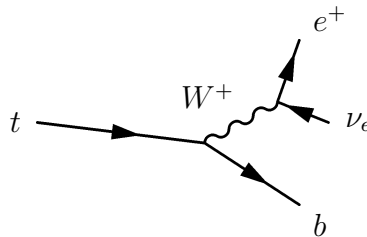


Figure 1.2: u-quark decaying into a d-quark, which is an example of lepto-quark weak decays.

Left-handed and right handed states transform differently under SU(2), the right handed leptons, e_R^- are electroweak singlets and the left-handed leptons are partnered with left-handed neutrinos as doublets.

¹U(1) is an abelian group of 1×1 unitary matrices.

²SU(2) is a non-abelian group of 2×2 unitary matrices with determinant 1.

$$\begin{pmatrix} \nu_l \\ l^- \end{pmatrix}_L \quad (1.1)$$

Electroweak symmetry breaking is necessary to explain the mixing of the electroweak gauge bosons, resulting in electroweak mass eigenstates, γ , W^\pm and Z^0 . Here, Y is the generator for $U(1)$ transformations related to the covariant derivative, $\mathcal{D}_\mu = \delta_\mu - i\frac{e}{2}YB_\mu$, responsible for the electromagnetic interaction and B_μ is the associated vector field. Y is defined as $Y = 2(Q - I^3)$ where I^3 is the third component of the weak isospin. σ^a is the generator for $SU(2)$ transformations responsible for weak interactions and W_μ its associated vector field coming from the corresponding covariant derivative term $-i\frac{g_2}{2}W_\mu^a\sigma^a$ with σ^a ($a = 1, 2, 3$) being Pauli matrices.

$$\begin{pmatrix} A_\mu \\ Z_\mu \\ W_\mu^+ \\ W_\mu^- \end{pmatrix} = \begin{pmatrix} \cos\theta_W & \sin\theta_W & 0 & 0 \\ -\sin\theta_W & \cos\theta_W & 0 & 0 \\ 0 & 0 & 1 & 1 \\ 0 & 0 & 1 & -1 \end{pmatrix} \begin{pmatrix} B_\mu^0 \\ W_\mu^0 \\ W_\mu^1 \\ W_\mu^2 \end{pmatrix} \quad (1.2)$$

Left-handed quarks can also be defined similarly. Right-handed quarks, $d_{R\alpha}$, and $u_{R\alpha}$ are singlets.

$$\begin{pmatrix} u_\alpha \\ d_\alpha \end{pmatrix}_L \quad (1.3)$$

Quarks transform in the color $SU(3)$ space so the α index represents the three possible colours (red, green and blue) and anticolours. The gauge boson involved in this invariance is the gluon. It is massless like the photon but they carry the colour-charge (colour and anticolour) and they can change it.

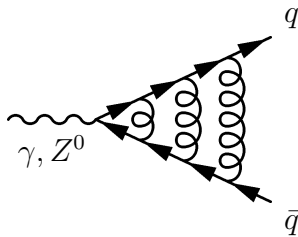


Figure 1.3: Quark antiquark production with gluon exchange.

Quarks and gluons can change both their momentum and colour charge by emitting or absorbing a gluon. Theoretically, gluons can interact among

themselves to form glueballs. This sets it apart from the photon. The Lund string model [12] describes quark interactions in Quantum Chromodynamics (QCD) specifically hadronization. Quark pairs are attached to each other by field lines (strings) that are compressed into tubelike regions. When the quark pairs are pulled away from each other, the strings break and form more quark pairs. This means that the quarks are confined inside hadrons. The energy supplied to pull them apart will be used to create a quark-antiquark pair thus making more hadrons. The strong interaction is responsible for keeping quarks together to form hadrons, which are either baryons or mesons. This makes the formation of stable baryons like the proton and neutron³ made from the lightest quarks, the u- and d-quarks possible.

The SM Lagrangian in Equation 1.8 describes elegantly all the $U(1) \times SU(2) \times SU(3)$ fermion-gauge boson interactions [58].

$$\mathcal{L} = \sum_{f=\nu_e, e, u, d} eQ_f(\bar{f}\gamma^\mu f)A^\mu \quad (1.4)$$

$$+ \frac{g_2}{\cos\theta_w} \sum_{f=\nu_e, e, u, d} [\bar{f}_L\gamma^\mu f_L(I_f^3 - Q_f \sin^2\theta_w) \quad (1.5)$$

$$+ \bar{f}_R\gamma^\mu f_R(-Q_f \sin^2\theta_w)]Z_\mu \quad (1.6)$$

$$+ \frac{g_2}{\sqrt{2}}[(\bar{u}_L\gamma^\mu d_L + \nu_{eL}\gamma^\mu e_L)W_\mu^+ + \text{h.c.}] \quad (1.7)$$

$$+ \frac{g_3}{2} \sum_{q=u, d} \bar{q}_\alpha\gamma^\mu \lambda_{\alpha\beta}^a q_\beta G_\mu^a \quad (1.8)$$

We have so far considered the first family of fermions (ν_e, e, u, d) but the theory can be applied to the next two families, (ν_μ, μ, c, s) and (ν_τ, τ, t, b) exchanging the same types of gauge bosons. The only difference is their mass and therefore their coupling strengths.

We assume there is a spin-0 Higgs fields that permeates all vacuum, $\phi_0 = \frac{1}{\sqrt{2}}(0, \nu)$, and we spontaneously break this symmetry, by letting $\nu \rightarrow \nu + H(x)$. The gauge bosons and fermions can interact with this fields and gain mass. For example, in Equation 1.9, the u - and \bar{u} - quark couple to the Higgs boson with a coupling strength of the $\frac{m_u}{\nu}$ giving it the correct mass.

$$\mathcal{L}_{int} = m_d\bar{d}d + m_u\bar{u}u + \frac{m_d}{\nu}\bar{d}dH + \frac{m_u}{\nu}\bar{u}uH \quad (1.9)$$

Gravitation as a fundamental force does not really fit into the Standard Model. Nevertheless, it is hypothesized that there may be gravitons, the

³Only stable inside nuclei.

1st family		2nd family		3rd family	
name	mass (MeV/c^2)	name	mass (GeV/c^2)	name	mass (GeV/c^2)
u	1.5 — 3.3	c	$1.27^{+0.07}_{-0.11}$	t	171.2 ± 2.1
d	3.5 — 6.0	s	$0.104^{+0.026}_{-0.034}$	b	$4.20^{+0.17}_{-0.07}$
e	0.511	μ	0.106	τ	1.777

Table 1.1: In the original formulation of the SM, neutrinos have zero mass. However, there is sufficient proof nowadays from neutrino oscillations that they have mass although we are not sure about their absolute values, only their mass differences between the neutrino flavours are known.

massless spin-2 gauge bosons that mediate the quantum theory of gravitation. So far, we have not found any evidence for it. As an illustration of how different the gravitational force is from other fundamental forces, the strong force is approximately 10^{38} times stronger, the electromagnetic force 10^{36} times stronger, and the weak force is 10^{25} times stronger than the gravitational force.

1.3 Limitations of the SM and Supersymmetry

There are several questions that could not be satisfactorily answered by the SM. A few of them are the strong CP problem [59], neutrino oscillations [66], the hierarchy problem and dark matter [68].

It is also clearly not a complete theory of fundamental interactions because it does not incorporate the physics of general relativity, such as gravitation and dark energy. The theory does not contain any viable dark matter particle that possesses all of the required properties deduced from observational cosmology. It is observed that there are unseen mass in the galaxy that is causing anomalies in galactic rotation. CP violation appears to be present in weak decays but almost non-existent in strong processes. Neutrino oscillations and mass are also not accounted for in the original form of the SM Lagrangian, which has been somewhat solved by adding in the missing mass terms.

Interaction strength of the fundamental forces give a clear picture of how different they are. It is described by the coupling constants which is actually a misnomer since they are not constants but vary with energy. The electromagnetic interactions are governed by the fine structure constant, $\alpha = \frac{e^2}{4\pi} = \frac{1}{137}$ at low energies. The weak interactions at low energies compared to the gauge boson mass is given by the Fermi constant, $G_F = 1.167 \times 10^{-5} GeV^{-2}$ and the

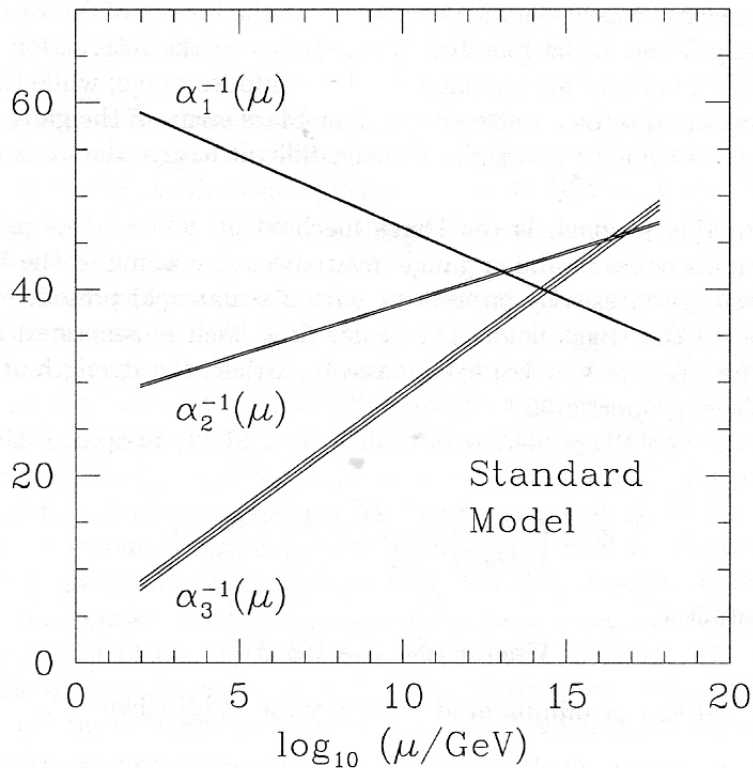


Figure 1.4: Running of couplings in the SM. The coupling strengths of the three fundamental forces do not unify when extrapolated to a higher energy but comes suggestively close.

strong coupling constant for strong interactions is given by $\alpha = \frac{g_s^2}{4\pi}$. When extrapolated to high energies, as shown in Figure 1.4, the coupling strengths of the SM do not converge in a single point.

The hierarchy problem can be seen in many comparisons but is clearest when asking why the Higgs boson is so much lighter than the grand unification energy ($m_{GUT} = 10^{16}\text{GeV}$), where one needs too much fine-tuning to cancel the radiative corrections and the bare mass of the boson. Let the mass squared of the Higgs boson be

$$\begin{aligned} m_H^2 &= m_0^2 + \Delta m_H^2 \\ &\approx m_0^2 - g\Lambda^2 \end{aligned} \tag{1.10}$$

where we have the bare Higgs mass, m_0^2 and the loop corrections to it as Δm_H^2 . If Λ is of the order of m_{GUT} then we will have a situation where the

bare Higgs mass and its loop corrections, each $\approx 10^{30}\text{GeV}$ to be fine-tuned and produce $m_H^2 \approx 10^2\text{GeV}$. Figure 1.5 is one of many loop diagrams that contribute to the Higgs boson's own mass.

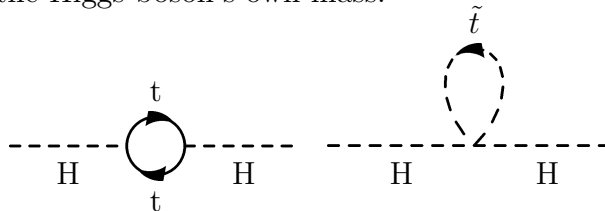


Figure 1.5: The Higgs boson quadratic mass one-loop contributions that cancel each other, fermionic top quark loop and scalar stop squark tadpole diagrams from a supersymmetric extension of the SM

Fermions that couple to the Higgs boson have a Yukawa coupling λ_f . This gives a Lagrangian, $L_{Yukawa} = -\lambda_f \bar{f} f H$, where f is the Dirac or fermion field and H the Higgs field. The Higgs will couple most strongly to the most massive fermion, the top quark. The quantum corrections to the Higgs mass squared is

$$\Delta m_H^2|_f = \frac{\lambda_f^2}{8\pi^2} [-\Lambda^2 + 6m_f^2 \log \frac{\Lambda}{m_f}] \quad (1.11)$$

The Λ is called the ultraviolet cutoff and represents the scale up to which the SM theory is valid. If we increase this to the GUT scale, m_{GUT} then we have the quadratically diverging Lagrangian. SUSY offers a solution to this problem such that if we consider that there exist complex scalars with spin-0,

$$\Delta m_H^2|_S = 2 \frac{\lambda_S^2}{16\pi^2} [\Lambda^2 - 2m_S^2 \log \frac{\Lambda}{m_S}] \quad (1.12)$$

This gives a total contribution to the Higgs mass to be zero if we include both fermionic and bosonic particles, suggested by the condition $\lambda_S = |\lambda_f|^2$ that can kill off the quadratic divergencies. This is what a supersymmetric transformation could do. It turns a bosonic state into a fermionic one and also the other way around. The operator Q that generates such transformations must be a anticommuting spinor,

$$Q|Boson\rangle = |Fermion\rangle \quad (1.13)$$

$$Q|Fermion\rangle = |Boson\rangle \quad (1.14)$$

Spinors are complex objects, so Q^\dagger is also a symmetry generator. They both carry half spin angular momentum, so it is clear that supersymmetry (SUSY) must be a spacetime symmetry. The supersymmetric single-particle states can be organized into irreducible representations, or supermultiplets⁴ which contain both fermion and boson states which are superpartners of each other.

The Minimal Supersymmetric Standard Model (MSSM) is the SM extension with the least changes such that SUSY can be incorporated. (There is a slight change in the Higgs sector: instead of a single Higgs boson: there must be five: h^0 , H^0 , H^+ , H^- and A^0 .) We then postulate a superpartner for every SM particle with the same coupling strengths. The SM particle and its SUSY partner differ only by its spin, and they should share the same mass. However, we did not for example, find the SUSY partner of the electron, the selectron, \tilde{e} with a mass of 0.511 MeV so this symmetry must be broken.

Another problem with the MSSM is that unfortunately, its 105 parameter leads to a lack of predictive power. Just as the masses in the SM all the particle masses are arbitrary and must be measured, the same is true in the MSSM. Here, constrained models like the minimal Super GRAvity (mSUGRA) are studied where only five parameters are needed.

1.4 Soft SUSY breaking

SUSY introduces many superpartners to the SM particles to enable the cancellation of quadratically divergent Λ present in the Higgs mass radiative correction equation, 1.11. In unbroken SUSY, the quadratic divergences vanish, but for broken SUSY, we need the couplings to be related as $\lambda_S = |\lambda_f|^2$. Thus it requires SUSY breaking to be soft, meaning the cancellation of quadratic divergences is maintained but it only contains mass terms and positive coupling parameters. The effective Lagrangian is then $\mathcal{L} = \mathcal{L}_{SUSY} + \mathcal{L}_{soft}$ ⁵ where

$$\mathcal{L}_{soft} = -\left(\frac{1}{2}M_a\lambda^a\lambda^a + \frac{1}{6}a^{ijk}\phi_i\phi_j\phi_k + \frac{1}{2}b^{ij}\phi_i\phi_j + t^i\phi_i\right) + \text{c.c.} - (m^2)_j^i\phi^{j*}\phi_i \quad (1.15)$$

⁴For example, a left chiral superfield looks like (Q, U^c, D^c, L, E^c)

⁵ \mathcal{L}_{SUSY} is similar to \mathcal{L}_{SM} only that there are extra terms from SUSY particles.

with gaugino masses M_a for each gauge group, scalar squared-mass terms $(m^2)_i^j$ and b^{ij} , (scalar)³ couplings a^{ijk} c_i^{jk} and tadpole coupling t^i , see Figure 1.5.

Chapter 2

SUSY models

2.1 MSSM

The MSSM is a straightforward supersymmetrization of the SM. It keeps the number of superfields and interactions as small as possible. The SM fermions are placed in different superfield from the gauge bosons. One generation of the SM is described by five left chiral superfields.

$$(Q, U^c, D^c, L, E^c) \quad (2.1)$$

where Q contains the (s)quark $SU(2)$ doublets, U^c, D^c contain the (s)quark singlets, L the (s)lepton doublets, E^c the (s)lepton singlets. There are also vector superfields to describe the gauge sector. Eight gluinos, \tilde{g} partnering the SM gluons, g , three winos, \tilde{W} , as partners to the W^\pm and Z^0 bosons and a bino, \tilde{B} as a $U(1)_Y$ gaugino. The winos and bino are not mass eigenstates but they mix together with the neutral Higgsino, \tilde{H}_0 to form four neutralinos, $\tilde{\chi}_i$ and two charginos, \tilde{C}_i^\pm .

To complete the description of the MSSM, we need to specify the soft supersymmetry breaking terms [25]. We have the Lagrangian that looks like

$$\begin{aligned} \mathcal{L}_{soft}^{MSSM} = & -\frac{1}{2}(M_3\tilde{g}\tilde{g} + M_2\tilde{W}\tilde{W} + M_1\tilde{B}\tilde{B} + c.c) \\ & - (\tilde{u}a_u\tilde{Q}H_u - \tilde{d}a_d\tilde{Q}H_d - \tilde{e}a_e\tilde{L}H_d + c.c.) \\ & - \tilde{Q}^\dagger\mathbf{m}_Q^2\tilde{Q} - \tilde{L}^\dagger\mathbf{m}_L^2\tilde{L} - \tilde{u}\mathbf{m}_u^2\tilde{u}^\dagger - \tilde{d}\mathbf{m}_d^2\tilde{d}^\dagger - \tilde{e}\mathbf{m}_e^2\tilde{e}^\dagger \\ & - m_{H_u}^2 H_u^* H_u - m_{H_d}^2 H_d^* H_d - (bH_u H_d + c.c) \end{aligned} \quad (2.2)$$

In Equation 2.2, M_1 , M_2 and M_3 are the bino, wino and gluino mass terms. The squark and slepton mass terms, (m_i^2) is a 3×3 hermitian matrix. $m_{H_u}^2$

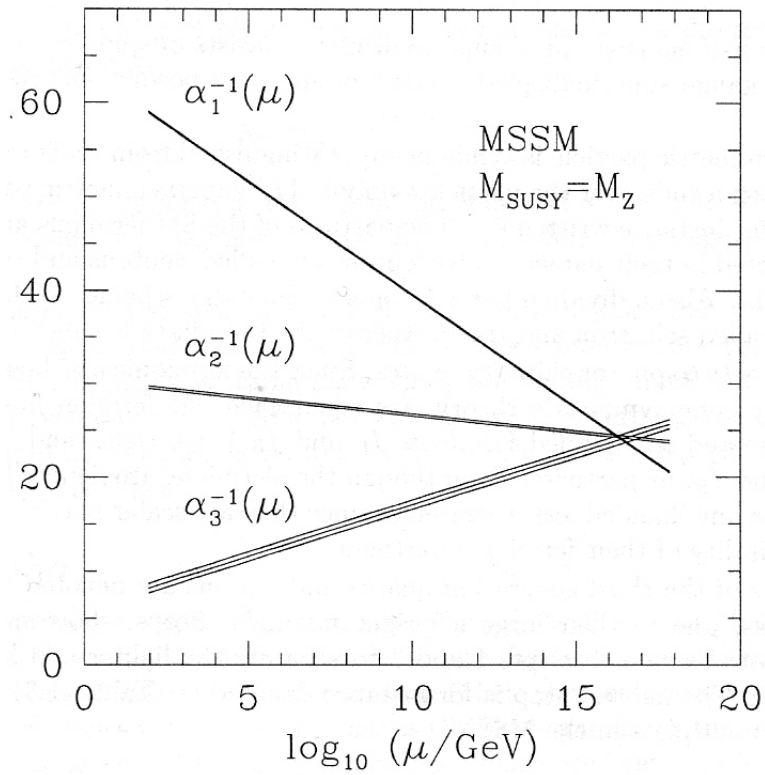


Figure 2.1: Running of couplings after introducing supersymmetry into the SM. Compared to the plot for SM, the extrapolated lines in SUSY converge to a single point.

and $m_{H_d}^2$ are the Higgs potential supersymmetry-breaking terms. The a_u , a_d and a_e terms are also complex 3×3 matrix corresponding to the Yukawa couplings of the superpotential. There are in total 105 masses, phases and mixing angles in the MSSM Lagrangian that cannot be rotated away by redefining the phases and flavor basis for the quark and lepton supermultiplets.

In addition, there are an additional three types of soft breaking terms [60]

- gaugino mass terms — $\frac{1}{2}m_l\bar{\lambda}_l\lambda_l$
- bilinear terms — $B_{ij}\phi_i\phi_j + h.c.$
- linear terms — $C_i\phi_i$

2.1.1 Electroweak symmetry breaking

In the MSSM, the description of EM symmetry breaking is relatively more complicated by the fact that there are two complex Higgs doublets $H_u = (H_u^+, H_d^0)$ and $H_d = (H_d^0, H_d^-)$. The classical scalar potential for the Higgs scalar fields in the MSSM [64] is

$$V = (|\mu|^2 + m_{H_u}^2)(|H_u^0|^2 + |H_u^+|^2) + (|\mu|^2 + m_{H_d}^2)(|H_d^0|^2 + |H_d^-|^2) \quad (2.3)$$

$$+ [b(H_u^+ H_d^- - H_u^0 H_d^0) + c.c.] \quad (2.4)$$

$$+ \frac{1}{8}(g^2 + g'^2)(|H_u^0|^2 + |H_u^+|^2 - |H_d^0|^2 - |H_d^-|^2) + \frac{1}{2}g^2|H_u^+ H_d^{0*} + H_u^0 H_d^{-*}|^2 \quad (2.5)$$

The terms proportional to $|\mu|^2$ come from the F-terms. The terms proportional to g^2 and g'^2 are the D-term contributions¹. The terms proportional to $m_{H_u}^2$, $m_{H_d}^2$ and b are a rewriting of the last three terms in 2.2. The minimum of this potential should break electroweak symmetry $SU(2)_L \times U(1)_Y \rightarrow U(1)_{EM}$. The Higgs fields get non-zero vacuum expectation values (VEV). Traditionally we can define the ratio as

$$\tan \beta \equiv \frac{\langle H_u^0 \rangle}{\langle H_d^0 \rangle} \quad (2.6)$$

We consider this quantity as it directly impacts the masses and mixing of the MSSM sparticles. The higgsinos and gauginos mix with each other

¹ $V(\phi_i) = |F_i|^2 + \frac{1}{2}\mathcal{D}^a\mathcal{D}^a$ where the F-terms and D-terms are $F_i \equiv \frac{\delta W}{\delta \phi_i}$ and $\mathcal{D}^a = -g(\phi_i^* T_{ij}^a \phi_j)$, useful for spontaneous symmetry breaking. The terms break SUSY if $\langle F_i \rangle \neq 0$ for some i . or the D-term, $\langle D_{l,a} \rangle \neq 0$ for some (l, a) .

due to electroweak symmetry breaking. The neutral higgsinos (\tilde{H}_u^0 and \tilde{H}_d^0) and the neutral gauginos (\tilde{B} and \tilde{W}^0) form four mass eigenstates called neutralinos, \tilde{N}_i^0 ($i = 1, 2, 3, 4$), which are analogous to the SM electroweak mass eigenstates. In the SUSY gauge basis, ($\tilde{B}, \tilde{W}^0, \tilde{H}_d^0, \tilde{H}_u^0$), we have the mixing matrix analogous to the one in Equation 1.2, $\mathbf{M}_{\tilde{\chi}}$ looking like [64]

$$\begin{pmatrix} M_1 & 0 & -\cos\beta \sin\theta_W m_Z & \sin\beta \sin\theta_W m_Z \\ 0 & M_2 & \cos\beta \cos\theta_W m_Z & -\sin\beta \cos\theta_W m_Z \\ -\cos\beta \sin\theta_W m_Z & \cos\beta \cos\theta_W m_Z & 0 & -\mu \\ \sin\beta \sin\theta_W m_Z & -\sin\beta \cos\theta_W m_Z & -\mu & 0 \end{pmatrix} \quad (2.7)$$

which can be diagonalized to get the mass eigenstates if we also consider at the limit $m_Z \ll |\mu \pm M_1|, |\mu \pm M_2|$ where $\tilde{\chi}_1^0 \approx \tilde{B}$, $\tilde{\chi}_2^0 \approx \tilde{W}^0$, $\tilde{\chi}_3^0, \tilde{\chi}_4^0 \approx \frac{1}{\sqrt{2}}(\tilde{H}_u^0 \pm \tilde{H}_d^0)$,

$$\begin{aligned} m_{\tilde{\chi}_1} &= M_1 - \frac{m_Z^2 s_W^2 (M_1 + \mu \sin 2\beta)}{\mu^2 - M_1^2} + \dots \\ m_{\tilde{\chi}_2} &= M_2 - \frac{m_W^2 (M_2 + \mu \sin 2\beta)}{\mu^2 - M_2^2} + \dots \\ m_{\tilde{\chi}_3}, m_{\tilde{\chi}_4} &= |\mu| + \frac{m_Z^2 (I - \sin 2\beta) (\mu + M_1 c_W^2 + M_2 s_W^2)}{2(\mu + M_1)(\mu + M_2)} + \dots, \\ &|\mu| + \frac{m_Z^2 (I + \sin 2\beta) (\mu - M_1 c_W^2 - M_2 s_W^2)}{2(\mu - M_1)(\mu - M_2)} + \dots \end{aligned} \quad (2.8)$$

Similarly, for the charged higgsinos (\tilde{H}_u^\pm ($i = 1, 2$) and \tilde{H}_d^\pm) and winos (\tilde{W}^+ and \tilde{W}^-) mix to form two mass eigenstates with charge ± 1 called charginos, \tilde{C}_i^\pm . The corresponding chargino mass eigenstates in the SUSY basis ($\tilde{W}^+, \tilde{H}_u^+, \tilde{W}^-, \tilde{H}_d^+$) are

$$\begin{aligned} m_{\tilde{\chi}_1^\pm} &= M_w - \frac{m_W^2 (M_2 + \mu \sin 2\beta)}{\mu^2 - M_2^2} + \dots \\ m_{\tilde{\chi}_2^\pm} &= |\mu| + \frac{m_W^2 (\mu + M_2 \sin 2\beta)}{\mu^2 - M_2^2} + \dots \end{aligned} \quad (2.9)$$

where $M_2 < |\mu|$, and I is the sign of μ . Experimentally, it is more useful to calculate the dilepton mass edge present due to the two-body kinematics [27],

Particles	Spin	R_P	Gauge Eigenstates	Mass Eigenstates
Higgs bosons	0	+1	$H_u^0 H_d^0 H_u^+ H_d^-$	$h^0 H^0 A^0 H^\pm$
squarks	0	-1	$\tilde{u}_L \tilde{u}_R \tilde{d}_L \tilde{d}_R$ $\tilde{s}_L \tilde{s}_R \tilde{c}_L \tilde{c}_R$ $\tilde{t}_L \tilde{t}_R \tilde{b}_L \tilde{b}_R$	(same) (same) $\tilde{t}_1 \tilde{t}_2 \tilde{b}_1 \tilde{b}_2$
squarks	0	-1	$\tilde{e}_L \tilde{e}_R \tilde{\nu}_e$ $\tilde{\mu}_L \tilde{\mu}_R \tilde{\nu}_\mu$ $\tilde{\tau}_L \tilde{\tau}_R \tilde{\nu}_\tau$	(same) (same) $\tilde{\tau}_1 \tilde{\tau}_2 \tilde{\nu}_{\tau\mu}$
neutralinos	1/2	-1	$\tilde{B}^0 \tilde{W}^0 \tilde{H}_u^0 \tilde{H}_d^0$	$\tilde{\chi}_1 \tilde{\chi}_2 \tilde{\chi}_3 \tilde{\chi}_4$
charginos	1/2	-1	$\tilde{W}^\pm \tilde{H}_u^\pm \tilde{H}_d^\mp$	$\tilde{\chi}_1^\pm \tilde{\chi}_2^\pm$
gluino	1/2	-1	\tilde{g}	(same)
goldstino(gravitino)	1/2 (3/2)	-1	\tilde{G}	(same)

Table 2.1: MSSM sparticles [64]

$$M_u^{max} = M(\tilde{\chi}_2^0) \sqrt{1 - \frac{M^2(\tilde{l}_R)}{M^2(\tilde{\chi}_2^0)}} \sqrt{1 - \frac{M^2(\tilde{\chi}_2^0)}{M^2(\tilde{l}_R)}} \quad (2.10)$$

2.2 mSUGRA

There are several models for breaking supersymmetry such as mSUGRA [24] and Gauge Mediated Symmetry Breaking (GMSB) [14]. mSUGRA breaks the symmetry in a hidden sector and mediates the SUSY breaking through gravity while GMSB SUSY breaking is mediated by a gauge interaction through messenger gauge fields. mSUGRA is a R-parity conserving theory. R-parity is defined as $R_P = (-1)^{2s+3B+L}$, with spin, s, baryon number, B and lepton number L. SM particles have R-parity 1 and SUSY particles have R-parity -1. For example the proton has $R_P = (-1)^{2(\frac{1}{2})+3(1)+0} = 1$, the electron, $R_P = (-1)^{2(\frac{1}{2})+3(0)+1} = 1$ and the $\tilde{\chi}_1^0$, $R_P = (-1)^{2(\frac{1}{2})+3(0)+0} = -1$. At the Grand Unified Theory (GUT), m_{GUT} scale, the parameters of MSSM are assumed to be unified which leads to the following relation of the free parameters of mSUGRA.

$$\begin{aligned}
g_1 = g_2 = g_3 &\equiv g_{GUT} & (2.11) \\
M_1 = M_2 = M_3 &\equiv m_{1/2} \\
m_Q^2 = m_U^2 = m_D^2 = m_L^2 = m_E^2 = m_{H_u}^2 = m_{H_d}^2 &\equiv m_0^2 \\
a_u = a_d = a_e &\equiv A_0
\end{aligned}$$

where g_i are the coupling constants, M_i are the SUSY fermion masses, m_j^2 are the SUSY scalar masses and A_0 is related to the Higgs-sfermion-sfermion Yukawa couplings. By using the mSUGRA equations above, we can now reduced the 105 MSSM parameters to only 5, the scalar masses, m_0 , the gaugino mass, $m_{1/2}$, soft breaking trilinear coupling constant (Higgs-sfermion-sfermion) A_0 , the ratio of the VEVs of the two Higgs, $\tan \beta$ and the sign of the Higgsino mass parameter (bilinear Higgsino coupling constant), $\text{sgn}(\mu)$. If R-parity is conserved and there is no lighter gravitino, there could exist a stable SUSY particle called the Lightest Supersymmetric Particle (LSP), which is the lightest neutralino, χ_1^0 . However, this particle is similar in detection difficulty to the neutrino since it only interacts weakly and gravitationally, therefore a hint for us to know it exists is to work out missing transverse energy (MET), \cancel{E}_T^2 from the detector. Momentum and energy is conserved therefore, by studying and measuring accurately the total momentum and energy of particles detected, we can infer from it the MET, see Equation 2.12.

$$\cancel{E}_T^2 = \cancel{E}_x^2 + \cancel{E}_y^2 \quad (2.12)$$

The $\cancel{E}_x^2 = \sum E_x^2$ and $\cancel{E}_y^2 = \sum E_y^2$ are the sum of all particles seen in the detector, for example, jets, muons, photons and electrons.

At the electroweak scale, squarks are heavier than sleptons. First and second generation squarks do not mix, but the third do. Due to mixing, \tilde{t}_1 , \tilde{b}_1 and $\tilde{\tau}_1$ are in the simplest models the lightest squarks/sleptons. Since squarks and sleptons decay into their SM partners if R-parity is conserved, τ s and b -jets are important to look for supersymmetric particles. The LSP can be a dark matter candidate if R-parity is conserved which can then be used to explain the observed missing mass of the universe. This particle needs to have a mass of between 100GeV and 1TeV, neutral and only interacts weakly and gravitationally. However, in the end, mSUGRA is limited since we now know that we need to probe larger regions in the SUSY parameter space. It may also be misleading if the theory used to explain experimental results are not realistic or general enough. Figure 2.3 shows a sample monte carlo generated invariant mass plot using benchmark point SU4. Figure 2.2 shows the explored and excluded regions in the mSUGRA parameter space.

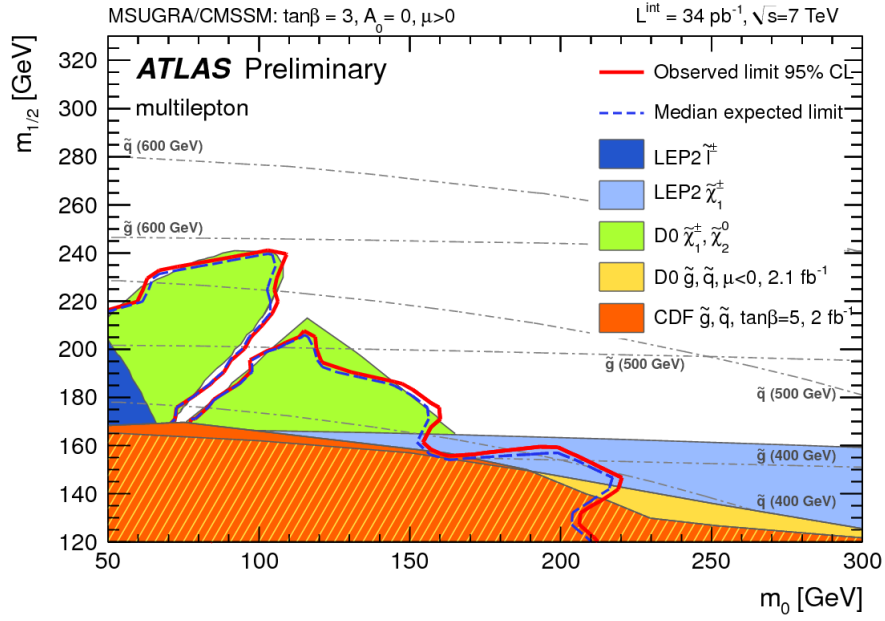


Figure 2.2: Observed and expected 95% C.L. exclusion limits in the $\tan\beta = 3, A_0 = 0, \mu > 0$ plane for mSUGRA.

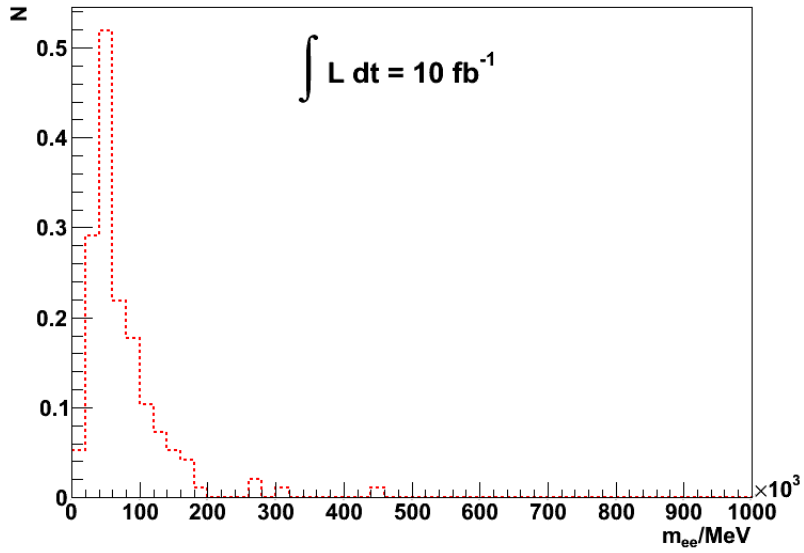


Figure 2.3: A sample mSUGRA SU4 benchmark point.

2.3 MSSM24

MSSM24 is a CP and flavour-conserving MSSM that has 24 parameters. High precision electroweak and B-physics collider observables and the dark matter relic density from WMAP4 results are used to constrain the parameter regions of the MSSM24 [8]. The MSSM24 parameters are shown in Table.2.2. There are two cases possible with this theory.

The first case is when the gluino/squark masses are within reach of the LHC energy. The initial pair usually $\tilde{g}\tilde{g}$, $\tilde{g}\tilde{q}$, $\tilde{q}\tilde{q}$. The decay of these (and subsequent decays) always produce several jets and LSPs give E_T^{miss} . The difference between this and mSUGRA is that mass differences can be smaller so the magnitude of p_T and E_T^{miss} can be modest. Lepton abundance is nearly fully tunable.

The second case describes \tilde{g} and \tilde{q} which are too heavy so the direct production of neutralinos/charginos/sleptons dominate. This is partly realisable in SU2 but with mass ratios, $m_{\tilde{g}} : m_{\tilde{\chi}_2^0} : m_{\tilde{\chi}_1^0} \approx 6 : 2 : 1$. This is more difficult to detect since the cross-sections for the processes will be smaller. There will be no hard jets and smaller E_T^{miss} .

Some signal grids available for study are the 4MassGrid and PhenoGrid. The 4MassGrid is a 4-dimensional grid of gluino, squark, χ_2^0 and χ_1^0 ranging from $(m_{\tilde{g}}, m_{\tilde{q}}, m_{\tilde{\chi}_2^0}, m_{\tilde{\chi}_1^0}) = (250, 200, 150, 100)$ to $(750, 700, 650, 600)$ GeV, with the condition that $m_{\tilde{g}} > m_{\tilde{q}} > m_{\tilde{\chi}_2^0} > m_{\tilde{\chi}_1^0}$ giving altogether 126 possible points. This grid is in use for 0-lepton searches and Higgses in cascades. The PhenoGrid, with 35 points is in use to study the 3-lepton channel searches. As an example, we have an dielectron invariant mass plot a phenoGrid sample in Figure 2.5. A mass edge at about 100GeV is present since the missing transverse energy is not taken into account.

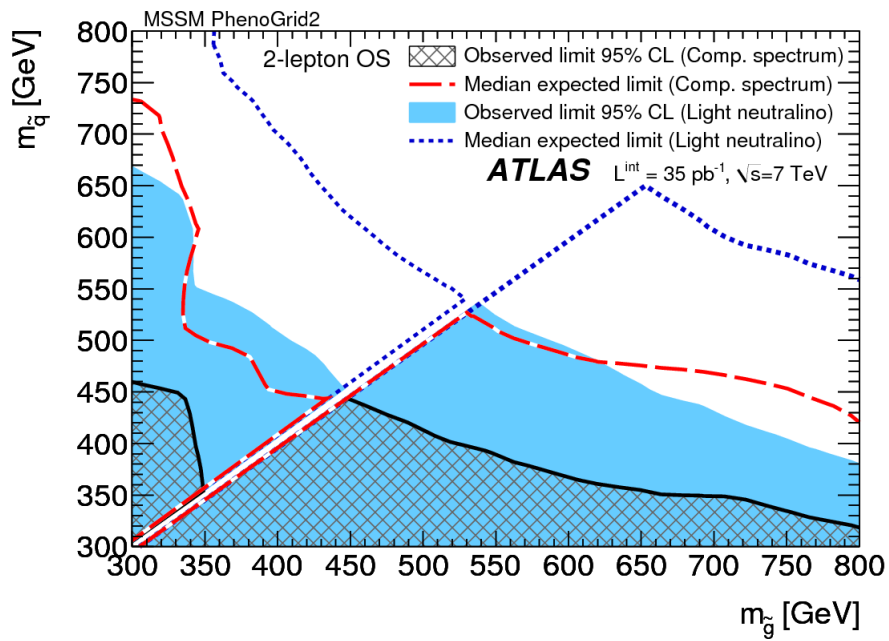


Figure 2.4: Observed and expected 95% C.L. exclusion limits in the $m_{\tilde{g}} = m_{\tilde{q}}$ plane for 24-parameter MSSM models.

Parameter	in mSUGRA	Description
M_1, M_2, M_3	$m_{1/2}$	Bino, Wino and Gluino masses
$m_{\tilde{e}_L} = m_{\tilde{\mu}_L}$	m_0	1st/2nd generation L_L slepton masses
$m_{\tilde{\tau}_L}$		3rd generation L_L slepton mass
$m_{\tilde{e}_R} = m_{\tilde{\mu}_R}$		1st/2nd generation E_R slepton masses
$m_{\tilde{\tau}_R}$		3rd generation E_R slepton mass
$m_{\tilde{u}_L} = m_{\tilde{d}_L} =$		
$m_{\tilde{c}_L} = m_{\tilde{s}_L}$		1st/2nd generation Q_L squark masses
$m_{\tilde{t}_L} = m_{\tilde{b}_L}$		3rd generation Q_L squark masses
$m_{\tilde{u}_R} = m_{\tilde{c}_R}$		1st/2nd generation U_R squark masses
$m_{\tilde{t}_R}$		3rd generation U_R squark mass
$m_{\tilde{d}_R} = m_{\tilde{s}_R}$		1st/2nd generation D_R squark masses
$m_{\tilde{b}_R}$		3rd generation D_R squark mass
m_t		top quark pole mass
$m_b(m_b)^{\overline{MS}}$		b-quark mass
$m_{H_{1,2}}$		up- and down-type Higgs doublet masses
$A_{t,b,\tau}$	A_0	top, b- and τ - quark trilinear couplings
$A_e = A_\mu$		μ and e trilinear couplings
$\tan \beta$	$\tan \beta$	scalar doublets VEVs ratio
$1/g_1(m_Z)^{\overline{MS}}$	g_{GUT}	electromagnetic coupling constant
$g_3(m_Z)^{\overline{MS}}$		strong coupling constant

Table 2.2: The 24 parameters of MSSM24. The SM parameters were taken as Gaussian noise around their mean experimental values: $m_t = 172.6 \pm 1.4$, $m_b(m_b)^{\overline{MS}} = 4.2 \pm 0.07$, $1/g_1(m_Z)^{\overline{MS}} = 127.918 \pm 0.018$ and $g_3(m_Z)^{\overline{MS}} = 0.1172 \pm 0.002$. [8]

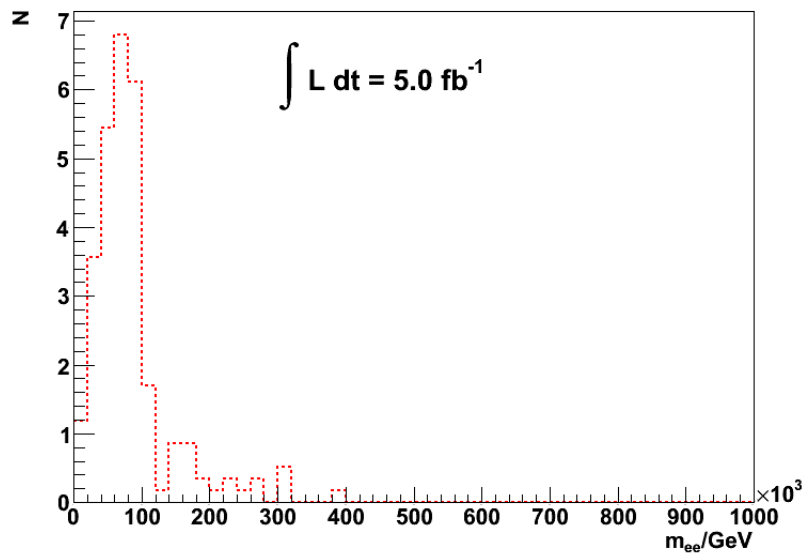


Figure 2.5: Invariant mass plot with $m_{\tilde{g}} = 300\text{GeV}$, $m_{\tilde{q}} = 310\text{GeV}$ and the LSP, $m_x = 100\text{GeV}$ in the 24-parameter MSSM model.

Chapter 3

LHC and the ATLAS Detector

The LHC started running in 2010 and has collected about 5.26 fb^{-1} of data by now. It is a proton-proton collider reusing the underground LEP tunnel (see Figure 3.2) around the Swiss-French border near Geneva. It is 27km in circumference and 50 to 175m below ground. The beams move around the LHC ring inside a continuous vacuum and bent around by powerful magnets (up to 8T). About 9300 superconducting magnets are cooled to about 1.9K. Since the LHC is circular, the charged particles that get accelerated by it lose synchrotron radiation. Since the LHC is circular, charged particles like the proton get accelerated and these particles lose energy via synchrotron radiation. The amount of energy loss is described by Equation 3.1.

$$\delta E \propto \frac{E^4}{m^4 R^2} \quad (3.1)$$

Since protons are composite particles, there is also a complication of multiple particle interactions (see Figure 3.1) due to QCD jets and also quarks carrying only a fraction of the center of mass energy.

In the LHC, the energy available in the collisions between the constituents of the protons (the quarks and gluons) is 7 TeV, although it is designed to operate at 14 TeV, compared to 200 GeV for LEP and the 2 TeV for the Tevatron. In order to maintain an equally effective physics programme at a higher energy E the luminosity of a collider (a quantity proportional to the number of collisions per second) should increase in proportion to E^2 . This is because the De Broglie wavelength associated to a particle decreases like $1/E$ and hence the cross section of the particle decreases like $1/E^2$. Whereas in past and present colliders the luminosity culminates around $L = 10^{33} \text{ cm}^{-2} \text{ s}^{-1}$, in the LHC it will eventually reach $L = 10^{34} \text{ cm}^{-2} \text{ s}^{-1}$. This will be achieved by filling each of the two rings with 2835 bunches of 1011

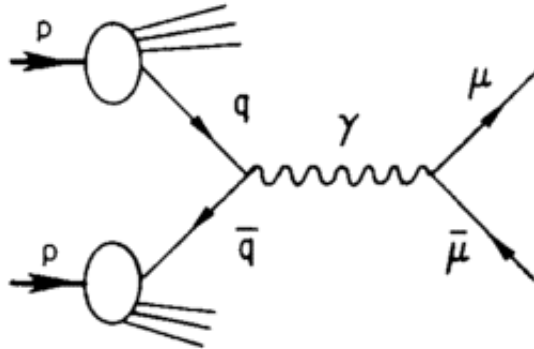


Figure 3.1: Proton-proton collision producing a muon-antimuon pair via photon exchange.

particles each. The resulting large beam current ($I_b = 0.53\text{A}$) is a particular challenge in a machine made of delicate superconducting magnets operating at cryogenic temperatures.

Due to the requirements of high luminosity and collision energy, there are some problems that are not present in lower energy accelerators. One of them is due to electrostatic same-charge repulsion. When two bunches cross in the center of a physics detector only a tiny fraction of the particles collide head-on to produce the wanted events. All the others are deflected by the strong electromagnetic field of the opposing bunch. These deflections, which are stronger for denser bunches, accumulate turn after turn and may eventually lead to particle loss. This beam-beam effect was studied in previous colliders, where experience showed that one cannot increase the bunch density beyond a certain beam-beam limit to preserve a sufficiently long beam lifetime. In order to reach the desired luminosity the LHC has to operate as close as possible to this limit. Its injectors, the old PS and SPS, are being refurbished to provide exactly the required beam density. The proton beams from the SPS are injected at 450 GeV and then accelerated to 7 TeV.

Another problem is related to close bunching of protons in the ring. There are 2835 bunches in the ring at any given time when the accelerator is running and they leave behind an electromagnetic wake-field which perturbs the next bunch following it. Under certain phase conditions, the proton oscillations in the transverse direction can be amplified and cause beam loss. This effect is minimized by a careful control of the electromagnetic properties of the elements surrounding the beam.

The protons need to be stored at high energy at a stable state for a long period of time. This is made difficult by protons that diffuse toward the

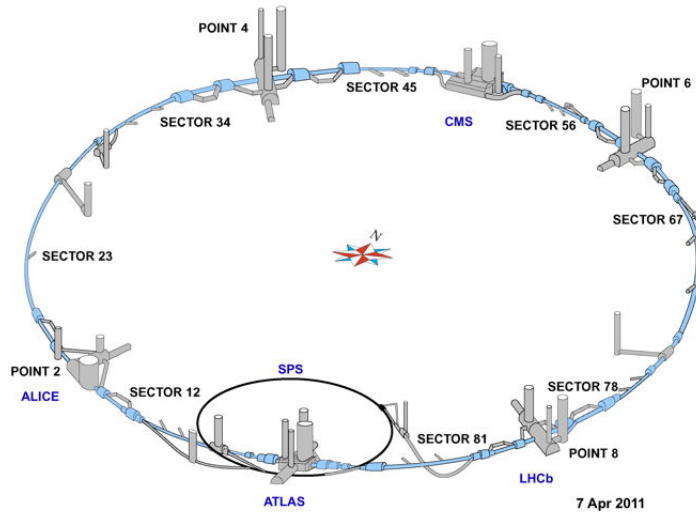


Figure 3.2: LHC underground structures.

beam pipe wall. The energy is lost into heat in the surrounding material and this may induce a quench of the superconducting magnets, interrupting operations for a few hours. Collimation systems are used to catch these stray protons.

Protons being accelerated in the LHC ring lose synchrotron radiation all the time. This loss is compensated by the RF systems around the ring, which add the energy back to the protons. Compared to e^+e^- colliders, the energy radiated is tiny but still is about 3.7kW and it has to be absorbed by the cryogenics, see Equation 3.1. The beams will then be stored at high energy for 10 to 20 hours, making about 400 million revolutions around the machine in 10 hours with collisions [19] take place inside the four main experiments, A Toroidal LHC ApparatuS (ATLAS), A Large Ion Collider Experiment (ALICE), Compact Muon Solenoid (CMS) and LHC beauty (LHCb).

ATLAS is a general purpose detector. It has multiple layers with each layer performing a specific task of detecting particle signatures. The layer closes to the interaction point is the Inner Detector (ID) which consists of the subdetectors: Pixel Detector, Semiconductor Tracker(SCT) and Transition Radiation Tracker (TRT). The next layer is the Electromagnetic Calorimeter (ECal) which is then covered by the Hadronic Calorimeter (HCal) and finally the Muon Spectrometer.

The ATLAS Collaboration aims at performing high precision test of QCD, electroweak interactions and flavour physics. The search for the Higgs boson, incorporating many production and decay channels over a large mass range

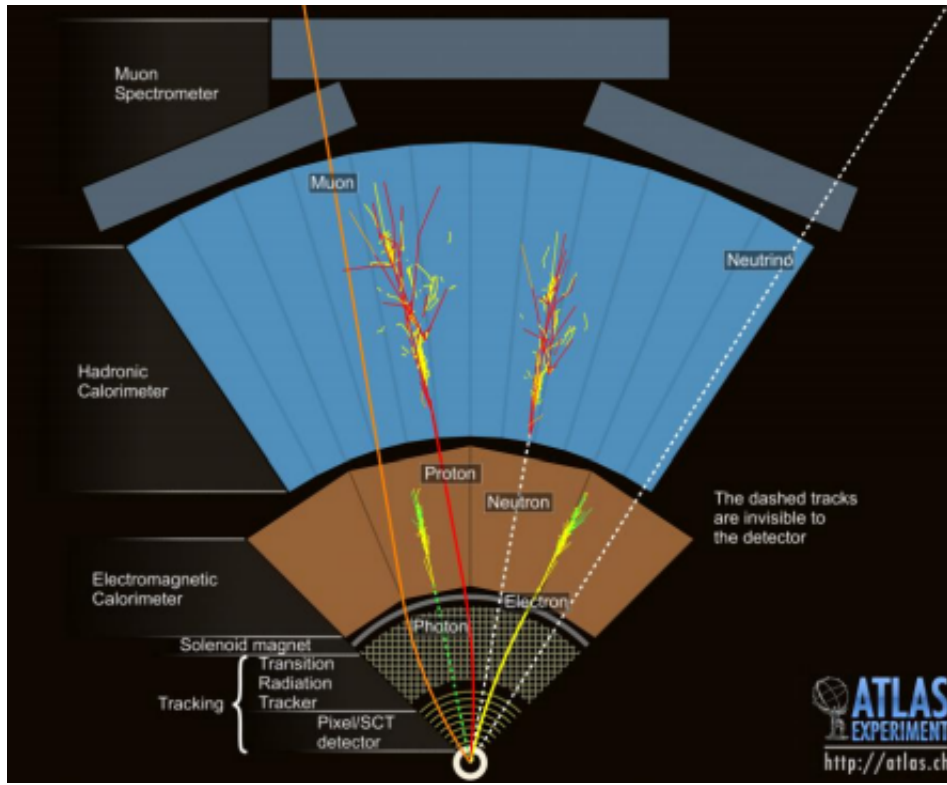


Figure 3.3: Tracks created by the many different particles created by the pp collision.

in part of that program. ATLAS is also used to study the SM and also physics beyond the SM such as Large extra dimensions, SUSY, R-hadrons and other exotic particles. Signatures of new physics are quite often provided by high- p_T jet and missing transverse energy measurements. The coverage of the ATLAS detector is almost hermetic¹, which means that almost all produced particles should be detectable and their positions and momenta well measured. It is then possible to infer from other known particle momentum, the missing transverse momentum providing clues to neutrino and neutralino momentum.

¹An ideal hermetic detector will have total solid-angle coverage, $\Omega \rightarrow 4\pi$.

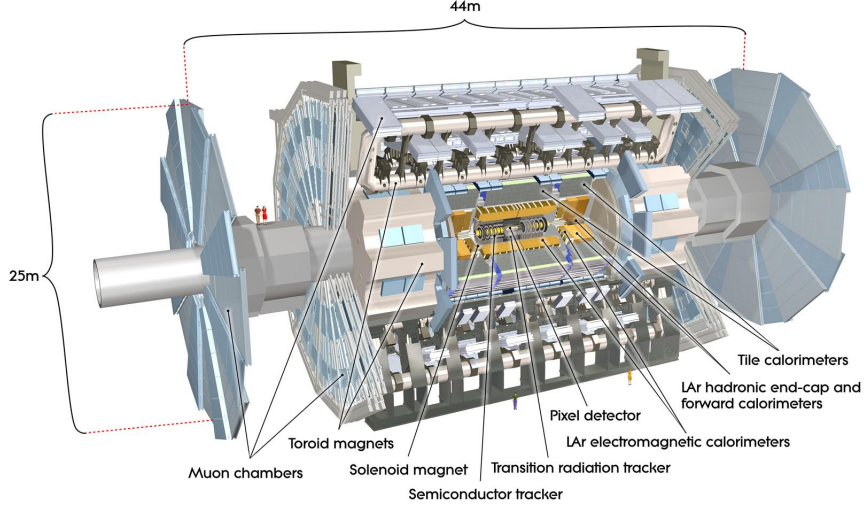


Figure 3.4: ATLAS detector [29]

Particle	Signature	Generic subsystem
$u, c, t \rightarrow W + b$ b, s, b g $\tau^+ \rightarrow \nu_\tau + c + s$	Jet of hadrons (λ_0)	ECal + HCal
e, γ	Electromagnetic shower (X_0)	Calorimeter ECal + trackers
ν_e, ν_μ, ν_τ $W \rightarrow \mu + \nu_\mu$	Missing transverse energy (MET)	ECal + HCal
$\mu, \tau \rightarrow \mu + \nu_\tau + \bar{\nu}_\mu$ $Z \rightarrow \mu + \mu$	Only ionization dE/dx	Muon spectrometer and trackers
c, b, τ	Secondary decay vertices	Vertex and trackers

Table 3.1: Particles of the SM and detection and identification in detector subsystems. In the ECal, high energy electrons lose energy in matter by radiating photons and photons will pair-produce. This means that after a certain length, called the radiation length, X_0 , the high-energy electron or photon will only retain $1/e$ of its original energy. The nuclear interaction length, λ_0 is a measure of the mean distance travelled by a hadronic particle before interacting inelastically with other hadrons.

3.1 The Inner Detector

The Inner Detector (ID) is contained within a cylinder of length 7 m and a radius of 1.15 m, in a solenoidal magnetic field of 2 T, see Figure 3.5. It consists of three subsystems: the Pixel detector, the Semiconductor Tracker (SCT) and the Transition Radiation Tracker (TRT). After the assembly of the ID, the position of the individual detector elements is known with less precision than their intrinsic resolution. The ID acts as a tracking system for charged particles. The highest granularity is achieved around the vertex region using semiconductor pixel detectors. The pixel and semiconductor trackers are silicon based detectors and the TRT is a drift chamber composed of straws filled with gas. A large number of tracking points (typically 36 per track) is provided by the TRT, which provides continuous track-following with much less material per point and a lower cost. All subsystems have a barrel part and two end-caps. The barrel parts consist of several layers of sensors while the end-caps are made of a series of disks or wheels of sensors. The ATLAS detector uses a Cartesian right-handed coordinate system with the interaction point being defined as the origin. The positive x -axis is defined as pointing from this interaction point to the center of the LHC ring, the positive y -axis pointing upwards, and the z -axis along the beam direction.

The helical trajectories of tracks are parametrised in the ATLAS software as five dimensional vectors, $\tau = (d_0, z_0, \phi_0, \theta, q/p)$ [26] where d_0 and z_0 are the transverse and longitudinal impact parameter respectively, measured with respect to the origin. ϕ_0 is the azimuthal angle of the track at the point of closest approach to the origin, and θ is the polar angle. The ratio q/p is the inverse of the particle momentum multiplied by its charge. The transverse momentum, p_T is computed as $p_T = p \sin \theta$. Finally, the particle pseudorapidity η is defined in terms of the polar angle θ which is $\eta = -\log \tan \theta/2$ [2].

3.2 Electromagnetic Calorimeter

The main task of an electromagnetic calorimeter (ECal) is to measure the energy of electrons and photons and to identify them in the large sea of hadrons. The ECal provides a redundant and destructive measurement of the electrons. It is the first of the calorimeters to be struck by outgoing particles from the collision. As compared to tracking and vertex systems, the calorimeter readout is destructive in that the showering particle is totally absorbed. The barrel ECal is contained in a cryostat which surrounds the

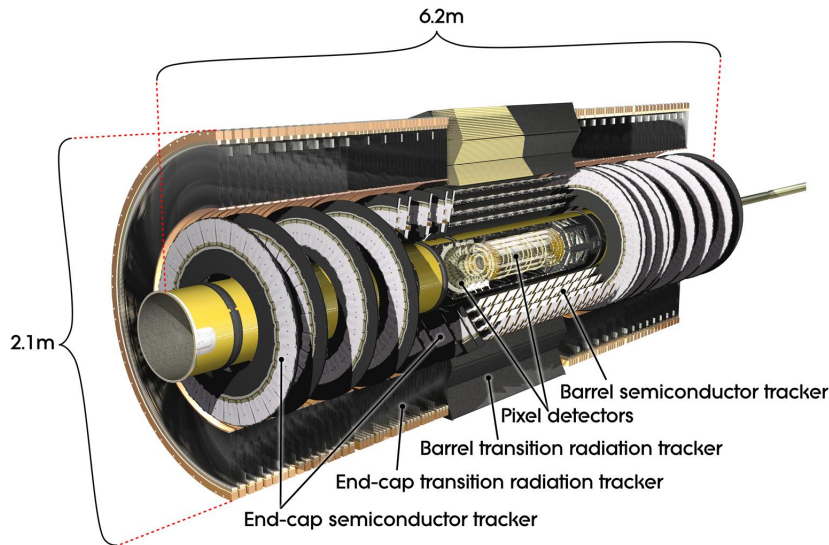


Figure 3.5: Inner detector [29]

ID cavity.

The ECal is divided into a barrel part with pseudorapidity coverage, $|\eta| < 1.475$ and two end caps, $1.375 < |\eta| < 3.2$. It is a liquid argon (LAr) detector [45]. LAr is intrinsically radiation resistant since it is a monoatomic noble gas but the disadvantage of using LAr is its slow response time. However, the LAr calorimeters are highly granular, with excellent performance in terms of energy and position resolution and covers the pseudorapidity range $|\eta| < 3.2$.

3.3 Hadronic Calorimeter

The hadronic calorimeter, HCal, measures the energy of strongly interacting quarks and gluons by absorbing jets of particles that these fundamental particles hadronize into. It measures the energy of all the secondary particles within a range of rapidity, $|y| < 5$, which is almost hermetic. This provides the calorimeter the ability to indirectly measure the missing transverse energy, MET to look for neutrinos [2].

The HCal consists of three main devices. In the barrel region ($|\eta| < 1.7$) there is the scintillating Tile Calorimeter. The Hadronic End-cap LAr Calorimeter (HEC) extends up to $|\eta| = 3.2$. The range $3.1 < |\eta| < 4.9$ is covered by the high density Forward Calorimeter (FCAL). Up to $|\eta| = 2.5$ the basic granularity of the hadron calorimeters is $\Delta\eta \times \Delta\phi = 0.1 \times 0.1$, see

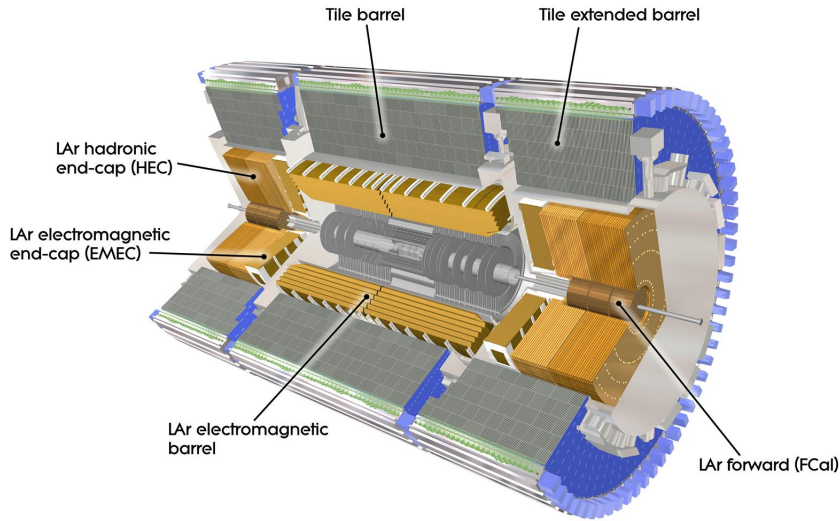


Figure 3.6: Calorimeters [29]

Figure 3.9. This region is to be used for precise measurements of the energy and angles of jets and, at low luminosity, of single charged particles. In the region $|\eta| > 2.5$, the basic granularity is approximately $\Delta\eta \times \Delta\phi = 0.2 \times 0.2$.

In the end-caps, the LAr technology is also used for the hadronic calorimeters, which share the cryostats with the EM end-caps. The same cryostats also house the special LAr forward calorimeters which extend the pseudorapidity coverage to $|\eta| = 4.9$. The bulk of the hadronic calorimetry is provided by a scintillator-tile calorimeter, which is separated into a large barrel and two smaller extended barrel cylinders, one on each side of the barrel. The overall calorimeter system provides a very good jet and MET performance of the detector. The LAr calorimetry is contained in a cylinder with an outer radius of 2.25m and extends longitudinally to ± 6.65 m along the beam axis. The outer radius of the scintillator-tile calorimeter is 4.25m and its half length is 6.10m. The total weight of the calorimeter system, including the solenoid flux-return iron yoke which is integrated into the tile calorimeter support structure, is about 4000 tons [2].

3.4 Muon Spectrometer

The HCal is surrounded by the muon spectrometer. The air-core toroid system, with a long barrel and two inserted end-cap magnets, generates a large

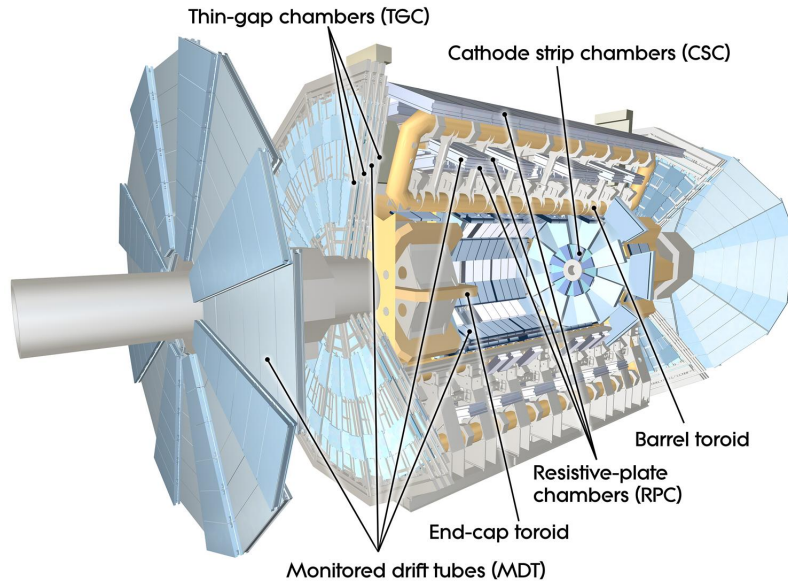


Figure 3.7: Muon chambers [29]

magnetic field volume with strong bending power within a light and open structure. Multiple-scattering effects are thereby minimised, and excellent muon momentum resolution is achieved with three stations of high precision tracking chambers. The muon instrumentation also includes as a key component trigger chambers with very fast time response. The muon spectrometer defines the overall dimensions of the ATLAS detector. The outer chambers of the barrel are at a radius of about 11 m. The half-length of the barrel toroid coils is 12.5 m, and the third layer of the forward muon chambers, mounted on the cavern wall, is located about 23 m from the interaction point. The overall weight of the ATLAS detector is about 7000 tons [2].

A major physics goal at the LHC is to explore vector boson interactions. Leptonic decays are favoured since they have little background and they can be cleanly and redundantly measured. Here, the muon can be first measured in the tracking system, deposit ionization energy in the calorimeters and end in the muon spectrometer. Muons at low transverse momentum originate from the decays of pions and kaons. They can be largely removed by requiring a good tracker fit to the hypothesis of no decay kink in the found track. Since the probability of decaying in the tracker falls with increasing momentum, pion and kaon decays are not a major problem in the LHC. A second source of muons is from heavy flavour decay, $b \rightarrow c + \mu + \nu_\mu$ which occurs faster and within the passage through the vertex detectors. The muon spectrometer

must produce a trigger so as to reduce the rate of background noises from the heavy flavour decays.

3.5 Triggers

In particle physics, a trigger is a system that uses simple criteria to rapidly decide which events in a particle detector to keep when only a small fraction of the total can be recorded. Trigger systems are necessary due to real-world limitations in data storage capacity and rates. Since experiments are typically searching for "interesting" events (such as decays of rare particles) that occur at a relatively low rate, trigger systems are used to identify the events that should be recorded for later analysis. The LHC has event rates of about 1 GHz and trigger rates of about 100Hz for permanent storage. The ratio of the trigger rate to the event rate is referred to as the selectivity of the trigger. For example, at the LHC, the Higgs boson is expected to be produced there at a rate of at least 0.01 Hz. Therefore the minimum selectivity required is 10^{-11} [62].

In the ATLAS detector, there are millions of events happening at the same time and there is a need to record interesting objects for example high p_T electrons, photons, jets, τ s decaying hadronically, muons, and events with large MET. The detector achieves this by a system of three levels of triggers. The Level 1 (L1) trigger is a hardware trigger that runs on dedicated processors (ASICs, FPGAs) mapped to the detector front-end electronics. Since the L1 Trigger must examine data at every bunch crossing (40 MHz), the full detector data is stored in a pipeline memory. It has a reasonable efficiency level of rejecting unwanted events at a good trigger rate with the criteria that the transverse energy, E_T deposit in the EM calorimeter in 1×2 trigger towers ($\Delta\eta \times \Delta\phi = 0.1 \times 0.1$) greater than 16 or 25 GeV for low and high luminosities respectively, see Figure 3.9. An additional criterion is to have E_T in a ring of 12 trigger towers surrounding the EM cluster to be less than 2 or 4 GeV for low and high luminosities respectively.

The event data are then transferred, after being accepted by the L1 trigger, to a series of memory buffers that store the data for use in Level 2 (L2) trigger processing. Then the L2 trigger which is mainly a software trigger takes over. More sophisticated algorithms are implemented and therefore the need for a longer decision time. Here, the event data is combined to form particle objects, e.g. τ made up of a thin jet and a track. The L2 trigger uses both information from the calorimeter and the inner detector which consequently allows for jet contamination and overlap reduction. For L2 Calorimeter triggering, the hadronic transverse energy, E_T in the window

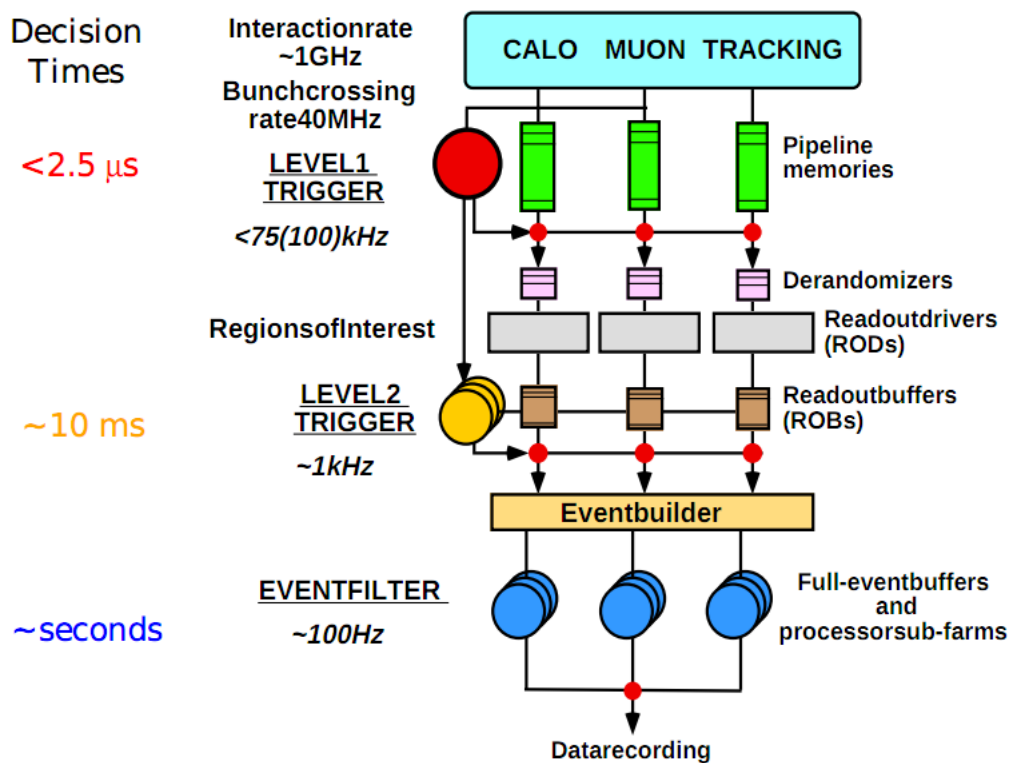


Figure 3.8: Overview of the ATLAS triggering system. [1]

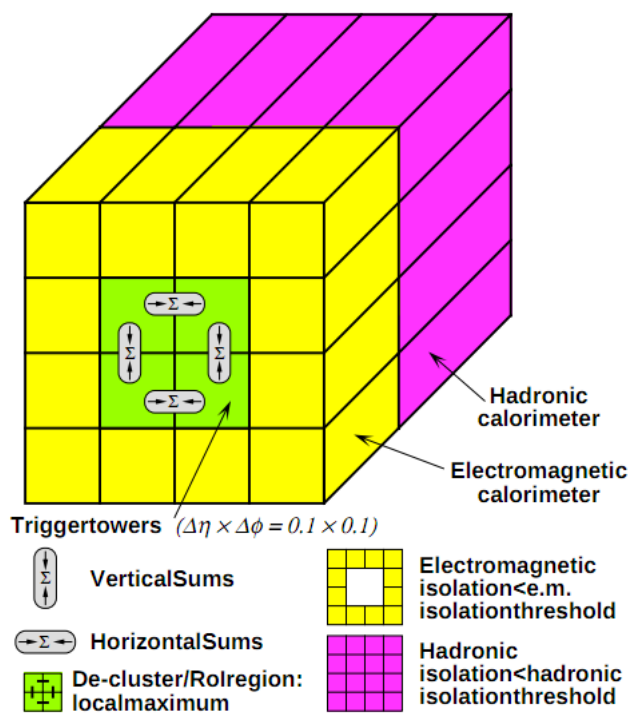


Figure 3.9: Calorimeter trigger towers.

of size $\Delta\eta \times \Delta\phi = 0.2 \times 0.2$ is constrained based on the E_T of the electron since jets can deposit a large fraction of the energy in the hadronic calorimeter. For inner detector selection of the L2 trigger, cuts are applied in the semiconductor tracker and the TRT to achieve a electron identification efficiency of about 83%. The events passing these cuts with showers having a large EM component are reduced due to the absence of a track reconstructed in the tracker.

The event filter is the last stage of the online event selection. It will tag events that will be written to mass storage by the data acquisition (DAQ) system for offline analysis. These events will be implemented in software running in commodity hardware. The aim is to reduce the L2 rate by about a factor of 10 in order to write the data at a rate of 100 MB/s. The strategy is to confirm the L2 decision and then use it as a starting point for further analysis.

3.6 Supersymmetric event displays

Figures 3.10 and 3.11 are some simulated events and how they will look like in the ATLAS detector. It requires the reconstruction of jets and precise measurements of electron, photon and muon momentum.

There are many ways in which hadronic jets can be reconstructed, and grouped into two kinds of algorithms, cones [49] and sequential. The cone algorithm maximizes p_T of the hadrons within a fixed cone size. The cone algorithm is not collinear and infrared safe. Infrared safe jets are invariant with respect to soft gluon emissions. There is cone algorithm called SIScone [69] which is both seedless and infrared safe.

There are three sequential algorithms, k_T , anti- k_T and the Cambridge-Aachen. The k_T algorithm [73] combines hadrons based on their distance, $d_{ij} = 2E_i E_j (1 - \cos \theta_{ij})$. However, the reconstructed jet cones are irregular.

The anti- k_T algorithm [22] is the default algorithm used by ATLAS to reconstruct jets with a distance parameter of 0.4. Using this algorithm, the high- p_T jets are merged first and the resulting reconstructed jets are regular as described in Equation 3.2. This algorithm is as good or better than all previous algorithms since it has linear response to soft particles.

The distance between the two particles, i and j is,

$$d_{ij} = \frac{\Delta R_{ij}^2}{\max(k_{ti}^2, k_{tj}^2)} \quad (3.2)$$

where $\Delta R_{ij}^2 = (y_i - y_j)^2 + (\phi_i - \phi_j)^2$ and k_{ti} , y_i and ϕ_i are respectively the transverse momentum, rapidity and azimuth of particle i .

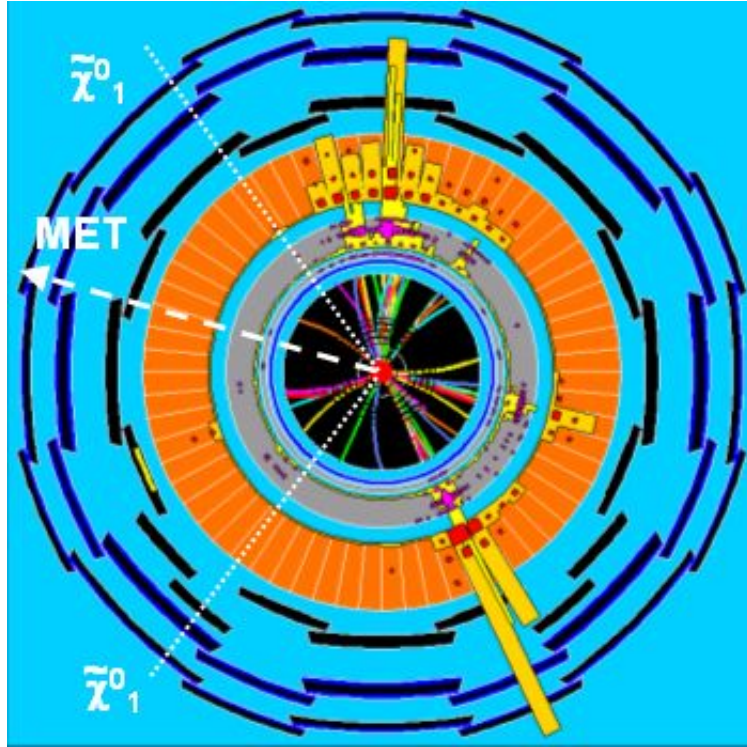


Figure 3.10: Simulated supersymmetric event in ATLAS. [29]

After reconstruction of jets, we now have information of all detectable particles (charged leptons, quarks and photons) which we can use this to calculate the missing transverse energy (MET), see Equation 2.12. For the second lightest neutralino, $\tilde{\chi}_2^0$ decay case, the detected particles would be two oppositely charged leptons and the LSP, $\tilde{\chi}_1^0$ that contributes to MET. As seen in Figure 3.10, the neutralinos escape undetected leaving behind missing transverse momentum.

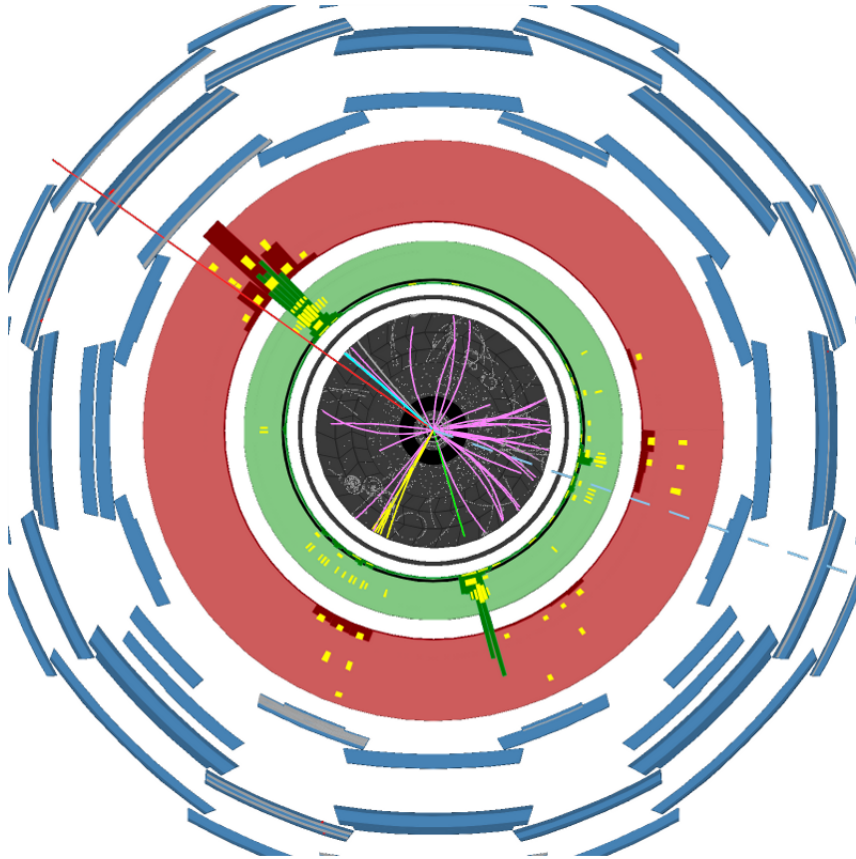


Figure 3.11: $t\bar{t}$ event display. The $t\bar{t}$ event is a major background source of $\tilde{\chi}_2^0$ decay into dileptons and missing energy. This particular event display is of a top pair $e\mu$ dilepton candidate with two b-tagged jets. The electron is shown by the green track pointing to a calorimeter cluster, the muon by the long red track intersecting the muon chambers, and the missing ET direction by the dotted line on the XY view. The secondary vertices of the two b-tagged jets are indicated by the orange bars.

Chapter 4

Grid Computing

High performance computing is required in modern scientific research as a way of solving computationally complex problems such as protein folding, weather forecasting and in high energy physics, particle hunting and data acquisition and storage. In addition to grid computing [52], there are many different competing technologies such as cloud computing and supercomputers. Grid computing links many different computer resources together via the internet making it fault tolerant and redundant such that no single system is a bottleneck. It achieves this using standard open source solutions like the Globus Toolkit [51], gLite [70] and ARC [47] and protocols like the Grid Security Infrastructure (GSI) to achieve a common goal.

4.1 WLCG

The Worldwide LHC Computing Grid (WLCG) is a distributed computing infrastructure to provide the production and analysis environments for the LHC experiments. It is managed and operated by a worldwide collaboration between the experiments and the participating computer centres with resources distributed across the world. The task is to make use of the resources available no matter where they are located. It is obvious that although it would be simpler to put all the resources in one or two large centres it is not a realistic option today. WLCG is therefore a distributed, or grid-based, infrastructure which is the most effective solution for meeting the data analysis challenge of this unprecedented scale. Currently WLCG is made up of more than 140 computing centers in 35 countries to process, analyze and store data produced from the LHC, making it equally available to all partners, regardless of their physical location.

WLCG is made up of four layers, or tiers; 0, 1, 2 and 3. Each tier provides

Region	Grid
Canada	TRIUMF
Germany	KIT
Spain	Port d'Informació Científica (PIC)
France	IN2P3
Italy	INFN
Nordic countries	Nordic Datagrid Facility
Netherlands	NIKHEF / SARA
Taipei	ASGC
United Kingdom	GridPP
USA	Fermilab-CMS
USA	BNL ATLAS

Table 4.1: Tier 1 sites.

a specific set of services.

Tier-0: This is the CERN Computer Centre. All data from the LHC passes through this central hub, but it provides less than 20% of the total compute capacity. CERN is responsible for the safe-keeping of the raw data (first copy), first pass reconstruction, distribution of raw data and reconstruction output to the Tier 1s, and reprocessing of data during LHC down-times.

Tier-1: These are large computer centres with sufficient storage capacity and with round-the-clock support for the Grid. They are responsible for the safe-keeping of a proportional share of raw and reconstructed data, large-scale reprocessing and safe-keeping of corresponding output, distribution of data to Tier 2s and safe-keeping of a share of simulated data produced at these Tier 2s. These eleven Tier 1 sites are shown in Table 4.1.

Tier-2: The Tier 2s are typically universities and other scientific institutes, which can store sufficient data and provide adequate computing power for specific analysis tasks. They handle analysis requirements and proportional share of simulated event production and reconstruction. There are currently around 140 Tier 2 sites covering most of the globe.

Tier-3: Individual scientists will access these facilities through local (also sometimes referred to as Tier 3) computing resources, which can consist of local clusters in a University Department or even just an individual PC. There is no formal engagement between WLCG and Tier-3 resources. LUNARC in Lund is an example of a Tier-3 computing facility.

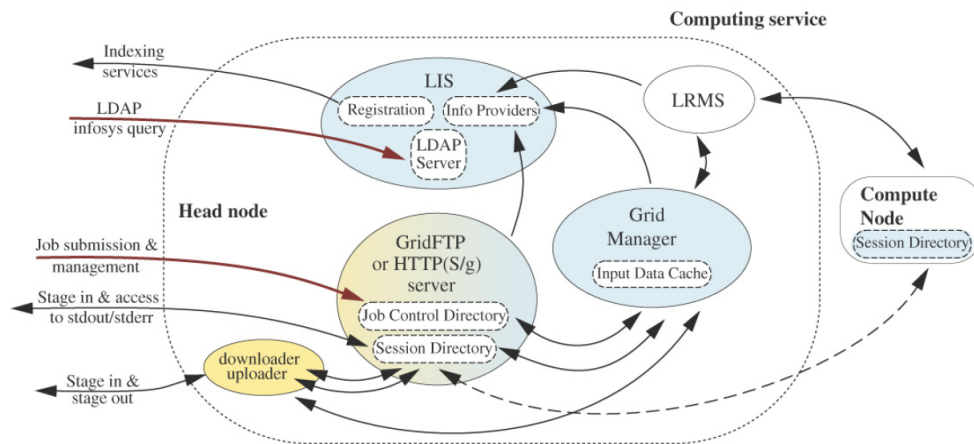


Figure 4.1: ARC Computing Service; arrows indicate data and information flow between the components.

4.2 NorduGrid and ARC

The most important task a grid must handle is probably the ability to handle massive amounts of data and heavy use of computing time. Nordugrid provides this capability with several computing centers located in Scandinavia and other parts of Europe. Another important feature is the existence of a simple, easy-to-install-and-use client. ARC provides the necessary functionality for the user to send and monitor jobs with minimal fuss.

Although WLCG and Nordugrid depends on the interconnectedness of various computers on the internet, it is novel software that enables the user to access computers distributed over the network. This middleware sits between the operating systems software of the computers and the physics applications software that solves a particular problem. It is a series of cooperating programs, protocols and agents designed to help users access the resources of a grid. Middleware is essential for WLCG to work - without it WLCG would not exist. The most important grid middleware stacks in WLCG are: EMI(ARC, gLite, UNICORE [16] and dCache [55]), Globus Toolkit, OMII [18] and Virtual Data Toolkit [48].

The Computing service as shown in Figure 4.1 is implemented as a GridFTP and has a Grid Manager (GM), as a more secure form of the usual FTP protocol. The GM is not present in other Grid middlewares. The GM is the main component of the service, providing an interface to the local resource management system. It also processes job descriptions written in Extended Resource Specification Language (XRSL) [46]. The GM is the core of the

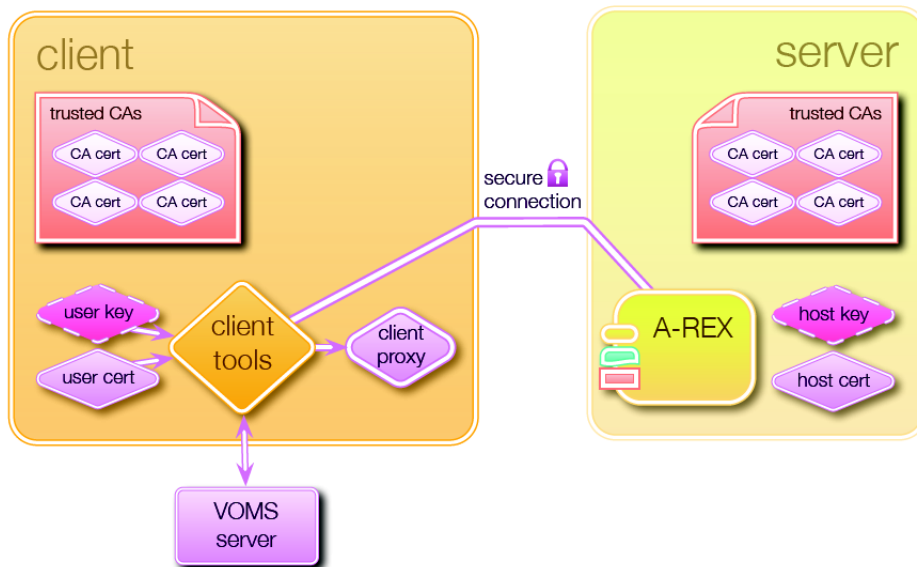


Figure 4.2: Certificates on the client side and on the server side. The client tools create a proxy certificate using the user’s credentials, and optionally collect more information about the Virtual Organization (VO) the user belongs by connecting to a Virtual Organization Membership Service (VOMS).

service as it executes jobs defined by the XRSL by gathering all input files, instructing the Local Resource Management System (LRMS) to run executables and transferring or storing the output files produced. It also has support for a variety of runtime environments, like the ATLAS software.

When the client submits a task, it polls the Information System (IS), which is a common distributed database and matches the user requirements to existing resources. The status of the job can also be queried by grid users using the ARC Command Line Interface (CLI). Grid users are those who are authorized to use at least one of the Grid resources by the means of Grid tools as described in Figure 4.2.

For users, all this complexity is hidden as they only need to formulate their tasks in XRSL and sends them to the grid along with their code, oblivious to the availability and location of computing or storage resources. The ARC middleware handles all the required tasks needed to send the user submitted files to the right cluster that will run the job requests.

While submitting jobs, users have to specify requirements for each job, namely, what software it should execute, what data to process, what kind of software environment it needs on the computing node, memory, CPU clock speed etc — these are specified in the formal job description. Various client

tools are available for example the native command-line interface by ARC middleware, GUI tools, web portals or specialized clients which are part of a bigger software tool. All users must be authenticated by grid services using X.509 certificates signed by trusted Certificate Authorities (CA). ARC also uses short-lived proxy certificates to delegate users' rights to various activities performed by Grid services on their behalf, such as job execution or data transfer. Authentication alone is not sufficient since users must also be authorized to perform such activities. Typically, users form groups (called Virtual Organizations, (VO)) to ease the process of getting authorized on the several computing resources [50].

4.3 Multithreaded processing on LXPLUS

WLCG provides access to computing resources which include data storage capacity, processing power, sensors, visualisation tools and more. There are a few methods that can be used by the user to send job requests for example Panda, and Ganga. The machines in the LXPLUS service are a cluster of PCs running Linux. They run SLC5 (Scientific Linux CERN 5) in 64 bit mode and are arranged in a load balanced cluster.

In LXPLUS machines, jobs can be sent for processing (in serial) using the `prun` command line tool which accepts customizations to it running properties by use of arguments to the program. This could be improved by using multithreaded programming written using interpreted languages like Python. This can drastically reduce processing time. Multiple threads are created by the Python interpreter to run `prun` for all the different datasets defined by the user. The program provides significant improvement when there are a lot more than one dataset to be processed. One dataset requires about 28.8 seconds to complete. Ten datasets run in series therefore takes about 300 seconds to complete. The same number run in parallel takes about 150 seconds to complete.

Sometimes, due to various intermittent problems like dataset unavailability at some storage elements certain datasets may fail to be read and the `prun` command may fail. The problem gets amplified especially in a parallel mode as the user may not notice the failing dataset. The Python code I have written could track these failed jobs and make it known to the user so that it may be sent again in the future, see Figure 4.3 for the process flow. The python Thread library is used to create multiple threads that run a `prun` subprocess. It then waits for the Ok status from `prun` to decide if the job is successfully submitted to the cluster or to write to file the dataset that failed to submit.

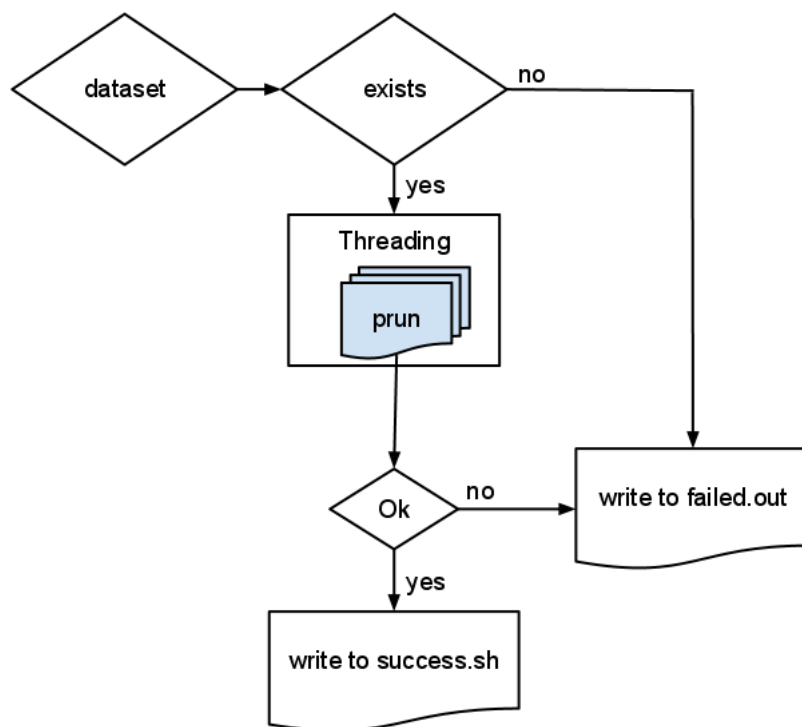


Figure 4.3: Each dataset is checked and processed using Python Thread library and submitted to the cluster by opening multiple threads of the prun subprocess.

4.4 Multithreaded arclib job submission

If the ATLAS software package is not available for the user, i.e. on the local machine, it is not possible to use Panda run (`prun`). The most straightforward way for running `prun` is as described in the previous section. There is also a significant hurdle in doing a proper installation and setup of the ATLAS software. As an alternative, it is possible to use ARC to query for ATLAS datasets and run analysis programs on the NorduGrid. The user is not restricted by the computing rules and limited resources of the LXPLUS clusters since the program runs in the local machine. However, it requires more work on the user's part such as finding the srm path locations of the datasets from AMI to analyse and also writing a XRSL file. I have also written a multithreaded python program for this purpose, see Figure 4.4 for the process flow.

Some of the advantages of using the arclib developer library are verification of matching return values from function calls, which is more rigid as compared to using regular expressions to parse the output of commands. It is also easy to avoid intermediate text files usually used to store parts of commands or file names. All this makes debugging and file management much more efficient.

4.5 Offline ROOT file operations

ARC commands provide a convenient way of list and downloading dataset files from the Storage Elements in the WLCG for testing on the local machine. However, it is required to know the srm link for it to work. This can be obtained by querying AMI to find the Storage Element name and then looking at the TiersOfAtlas.py python file.

There is also a convenient way of reading ROOT files directly from a dcache server. It requires the files from www.dcache.org/downloads/dcap. They are¹

```
libdcap
libdcap-devel
libdcap-tunnel-gsi
libdcap-tunnel-krb
libdcap-tunnel-ssl
```

ROOT needs to be setup with dcap support, using `-enable-dcache -with-dcap-inclDir=<path-to-include> -with-dcap-libdir=<path-to-lib>` and both

¹With root access, a simple yum install dcap would work.

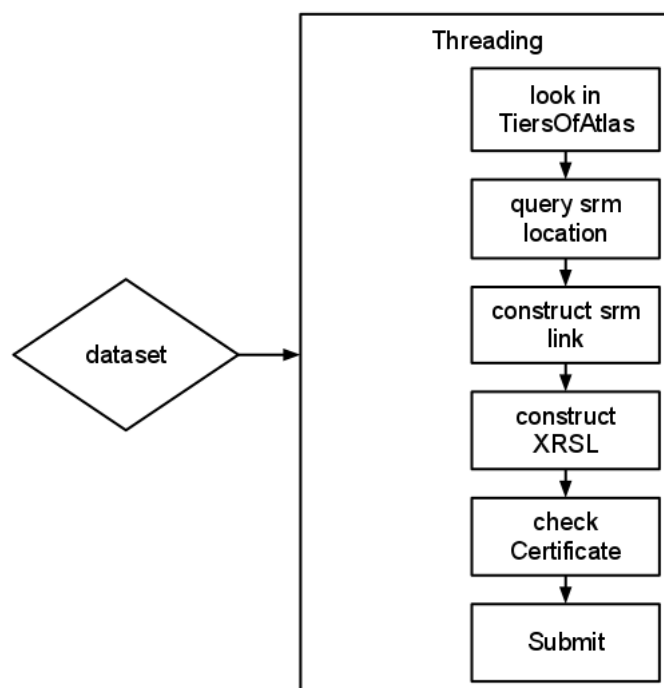


Figure 4.4: Almost similar to the process described in Figure 4.3 each dataset location(in this case, the srm location) is verified and the corresponding XRSL scriptis generated using Python Thread library and submitted via arclib.

the PATH and LD_LIBRARY_PATH environments updated to

```
export PATH=$PATH:<path-to-bin>  
export LD_LIBRARY_PATH=$LD_LIBRARY_PATH:<path-to-lib>
```

Chapter 5

Analysis

5.1 Finding the $\tilde{\chi}_2^0$

The second lightest neutralino, $\tilde{\chi}_2^0$, can decay via right-handed slepton or Z boson exchange into a lepton-antilepton pair and the lightest neutralino, which remains undetected by the ATLAS detector (missing energy). The $\tilde{\chi}_2^0$ can be produced from squark production in a pp collision, where the squark decays into a quark and $\tilde{\chi}_2^0$ as shown in Figure 5.1. In R-parity conservation, $\tilde{\chi}_1^0$ is the Lightest Supersymmetric Particle (LSP) which is a Dark Matter candidate. Here we will study opposite sign dielectron events as they have a relatively smaller background compared to hadronic processes hence a clearer signal. However, we need to consider MET due to neutrinos and neutralinos and lower statistics. This is because most of the decays of electroweak gauge bosons are quarks and antiquarks. However, this is compensated by the fact that electron and muon identification is less ambiguous than jets. There are a lot of events that involve jets but due to overlaps and cone sizes, it is not easy to define a jet. Some techniques do exist, like b-tagging for top quark identification purposes¹.

The ATLAS detector can record tracks and calorimeter signatures that are reconstructed as electron, muons, photons and jets. We therefore use them to look for new physics or perform more precise measurements of particle mass, momentum distribution and cross section from these leptons and jets. There are a few categories of searches we could perform as shown in Table 5.1.

Inclusive searches are not theory specific, and less optimized but are sensitive to a wider range of BSM physics. We consider the number of leptons or

¹b-tagging is the detection of b-hadrons to determine the jet due to the bottom quark and is crucial in identifying top quarks efficiently

Type	Description
0-lepton [35]	jets + \cancel{E}_T
1-lepton [36], [32]	single lepton + jets + \cancel{E}_T
OSDL [33], [34]	opposite sign dilepton + jets + \cancel{E}_T
SSDL [31]	same sign dilepton + jets + \cancel{E}_T
≥ 3 leptons	multilepton channel
2 photons [37]	diphoton + jet + \cancel{E}_T
γ + lepton	γ + lepton + \cancel{E}_T

Table 5.1: Beyond standard model search channels.

jets in the final state. It uses generic missing energy signatures and many include jet requirements to be sensitive to the strong parameter. For any type of searches, it is important to understand the background signal. Leptons here refer to electrons and muons. Taus decay leptonically (hence neutrinos) or hadronically (hence jets) therefore it is not easily identifiable.

An inclusive search with two same-sign leptons are interesting as there are a number of models predicting same-sign dilepton signals namely two descriptions of Majorana neutrinos [23], a cascade topology similar to supersymmetry or universal extra dimensions, and fourth generation down-type quarks [31]. These events are rare in the SM. One of the possible fake backgrounds from $t\bar{t}$ is non-isolated leptons from the weak decay of the bottom quark into a charm quark, lepton and antineutrino. An isolated lepton here would be one of the decay products of the top quark.

Inclusive searches with two opposite-sign leptons would constrain the descriptions of $\tilde{\chi}_2^0$, one of the neutralinos of MSSM, Z' [34], which is a new heavy spin-1 gauge boson of the Sequential Standard Model (SSM) [61] from one of the extensions of the SM. Here we are primarily interested in studying this signature to look for the $\tilde{\chi}_2^0$ which depends on the squark-gluino mass parameters. For example, the SU4 benchmark point places the $\tilde{\chi}_2^0$ mass at 113.48 GeV.

5.2 Monte Carlo Samples

MC datasets are generated using MC generators Alpgen, Pythia, Herwig and many others each with their own strengths. The generated events are sent to a GEANT4 simulation of the ATLAS detector to produce the expected particle tracks from these SM particles. Monte Carlo (MC) simulation samples are used to calculate the invariant mass with contributions from various

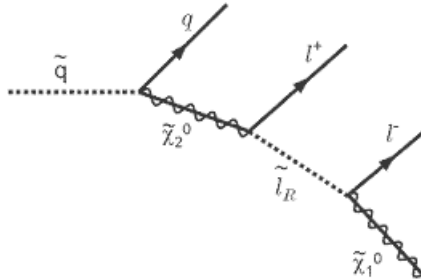


Figure 5.1: Squark cascade after pp-collision resulting in the creation of a $\tilde{\chi}_2^0$ which then decays into the LSP, $\tilde{\chi}_1^0$.

SM background processes. All MC samples are processed with the GEometry ANd Tracking (GEANT4) [9] simulation of passage of particles through the ATLAS detector [39] and events are passed through the same analysis chain as the data. An alternative way is to use ATLAS Fast (AtlFast) simulation package, but it skips the full detector simulation, digitization and reconstruction phases and runs smearing on the MC data instead. A simple flow chart in Figure 5.2 describes the processes that turn raw MC generated events to match detector readouts. The process ends at producing a Analysis Object Data (AOD) file that could already be used for analysis. The next possible layer is the D3PD files created from AODs contain ROOT variables that are easier to use. They are also available from many different ATLAS groups that do analysis work on different Beyond the Standard Model (BSM) signals.

The generation of SM Drell-Yan background events uses mainly ALPGEN MC multiple parton process generator using MLM matching scheme [63] and the CTEQ6L1 [67] PDF set. The Z/γ^* +jets samples are normalized to next-to-next to leading order (NNLO) with a k-factor² of 1.25 [27]. These simulated events are hadronised using the HERWIG [42], [43] shower model supplemented by the underlying event model JIMMY [21]. Both hadronization programs are tuned to the ATLAS MC10 tune [28]. Diboson WW, WZ and ZZ events are modelled using the ALPGEN generator normalized with k-factors of 1.26 (WW), 1.28 (WZ) and 1.30 (ZZ) to match the total cross section. Top antitop pair events are generator using Pythia [71] with POWHEG [54], [65], [53], [11] for implementing next to leading order (NLO) calculations in MC showers and normalized with k-factor of 1.129.

The Z +jets samples also contains full Drell-Yan contributions from the process $\gamma^* \rightarrow ll$ and takes the interference into account in addition to Z

²k-factor is the ratio of NNLO to the NLO values calculated theoretically.

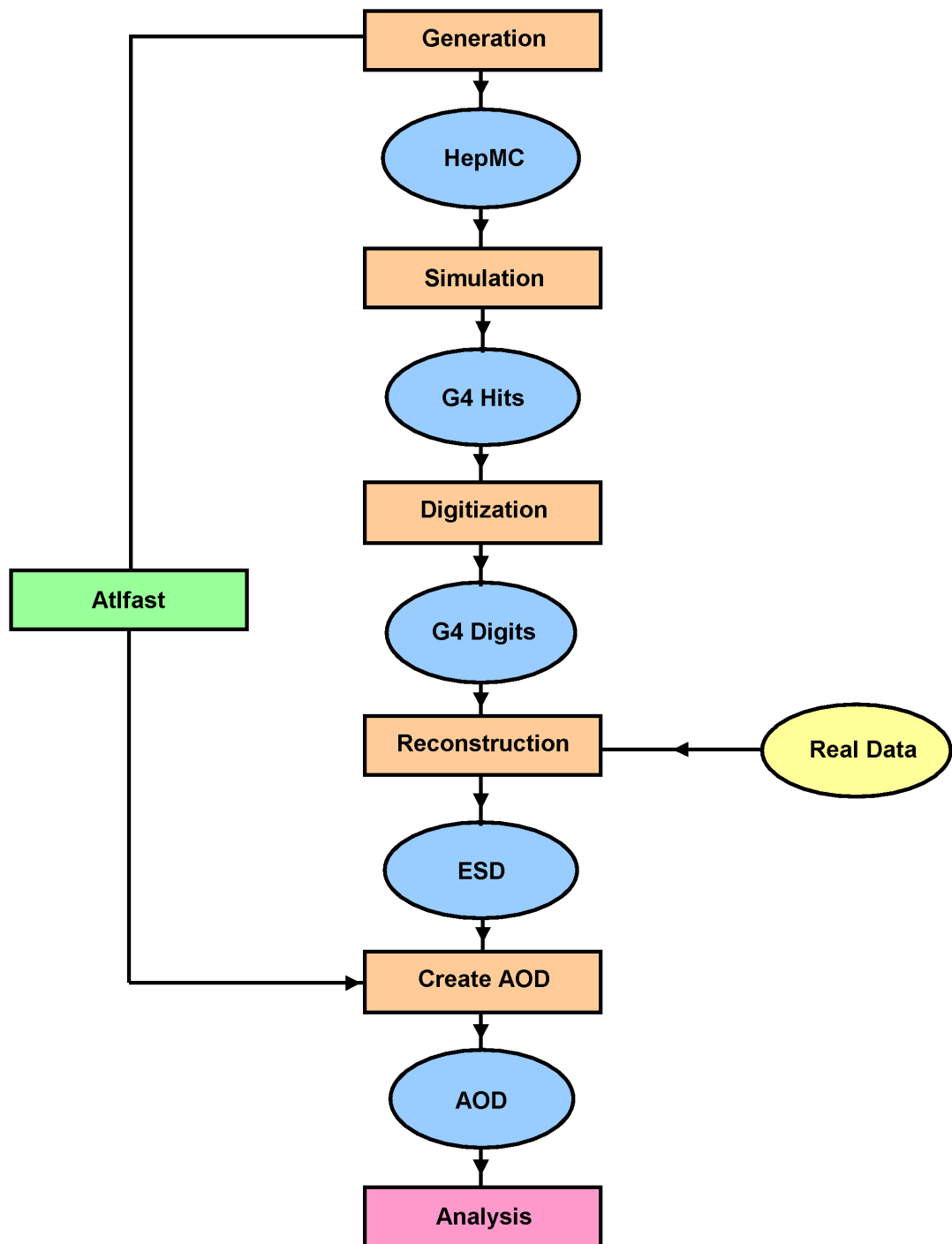


Figure 5.2: Full chain MC production. Real data from the ATLAS detector goes directly into reconstruction and ends up with the same types of variables with MC data.

Process	m_{ll} / GeV	σ / pb^{-1}	k-factor
$Z \rightarrow ee + 0 \text{ jet}$	> 40	668.32	1.25
$Z \rightarrow ee + 1 \text{ jet}$	> 40	134.36	1.25
$Z \rightarrow ee + 2 \text{ jets}$	> 40	40.54	1.25
$Z \rightarrow ee + 3 \text{ jets}$	> 40	11.16	1.25
$Z \rightarrow ee + 4 \text{ jets}$	> 40	2.88	1.25
$Z \rightarrow ee + 5 \text{ jets}$	> 40	0.83	1.25
$Z \rightarrow ee + 0 \text{ jet}$	$10 < m_{ll} < 40$	3055.20	1.25
$Z \rightarrow ee + 1 \text{ jet}$	$10 < m_{ll} < 40$	84.92	1.25
$Z \rightarrow ee + 2 \text{ jets}$	$10 < m_{ll} < 40$	41.40	1.25
$Z \rightarrow ee + 3 \text{ jets}$	$10 < m_{ll} < 40$	8.38	1.25
$Z \rightarrow ee + 4 \text{ jets}$	$10 < m_{ll} < 40$	1.85	1.25
$Z \rightarrow ee + 5 \text{ jets}$	$10 < m_{ll} < 40$	0.46	1.25
$W \rightarrow e\nu + 0 \text{ jets}$	> 40	6921.60	1.20
$W \rightarrow e\nu + 1 \text{ jets}$	> 40	1304.30	1.20
$W \rightarrow e\nu + 2 \text{ jets}$	> 40	378.29	1.20
$W \rightarrow e\nu + 3 \text{ jets}$	> 40	101.43	1.20
$W \rightarrow e\nu + 4 \text{ jets}$	> 40	25.87	1.20
$W \rightarrow e\nu + 5 \text{ jets}$	> 40	7.00	1.20
WW	no cut	11.5003	1.48
ZZ	no cut	0.9722	1.30
WZ	no cut	3.4641	1.60
$t\bar{t}$	no cut	79.17	1.129

Table 5.2: $Z \rightarrow ee + \text{jets}$ and $W \rightarrow e\nu + \text{jets}$ cross sections and k-factors.

events. The NLO k-factors for Alpgen Z+jets unfiltered samples are assumed to work with other Alpgen Z+(X)+jets samples. These samples have been generated with dileptons in the invariant mass range between 40 GeV and 200 GeV with a cross section as show in the Table 5.2 and normalized to the NNLO Z production cross section. The W+ Jets cross sections are also normalised to the NNLO W production cross section [20]. This is a sample containing W+light jets, W+charm (massless charm) and W+bb (where bb are produced in the parton shower).

As described in Chapter 2.2, the mSUGRA model is parameterized by just five constants, which makes it easy to tweak parameters. Table 5.3 shows the benchmark points [3].

- Coannihilation point — the $\tilde{\chi}_1^0$ is pure Bino. This region is where $\tilde{\chi}_1^0$ annihilate with near-mass degenerate \tilde{l} .

Point	Description	m_0	$m_{1/2}$	A_0	$\tan \beta$	$\text{sgn}\mu$	$\sigma_{LO} / \text{pb}^{-1}$
SU1	Coannihilation	70	350	0	10	+	8.15
SU2	Focus	3550	300	0	10	+	5.17
SU3	DC1 bulk region	100	300	-300	6	+	20.85
SU4	Low mass	200	160	-400	10	+	294.46
SU6	Funnel region	320	375	0	50	+	4.47
SU8.1	Coanni. variant	210	360	0	40	+	6.48

Table 5.3: Summary of the mSUGRA benchmark points chosen by ATLAS. These points are motivated by cosmological constraints. The SU4 low mass point has the lowest allowed SUSY masses and is used mainly by ATLAS as a benchmark. The cross-sections for the SUSY signal benchmark samples were calculated at the NLO using PROSPINO2.0.6 [15] and CTEQ6M [72] PDF functions.

- Focus point — the $\tilde{\chi}_1^0$ has a high Higgsino mixing component enhancing the annihilation cross-section for processes like $\tilde{\chi}_1^0 \tilde{\chi}_1^0 \rightarrow WW$, near $\mu^2 = 0$ bound with heavy sfermions.
- DC1 bulk region point — the $\tilde{\chi}_1^0$ is mostly Bino, annihilation happens with light sleptons exchange.
- Low mass — Large cross section but the events are similar to top quarks.
- Funnel region point — Wide H, A for $\tan \beta \gg 1$ that enhances annihilation. Hence, there is a heavy Higgs resonance and main annihilation chain into bb pairs. Tau decays are dominant.
- Coannihilation variant — mass of $\tilde{\chi}_1^0$ and $\tilde{\tau}$ similar.

In the MSSM24 model which is implemented as signal grid phenoGrid, phase space parameters chosen to be studied are a combination of scans in $(m(\tilde{q}_L), m(\tilde{g})) = (300, 400, 500, 600) \times (300, 400, 500, 600)$ which are 16 combinations in total.

The PhenoGrids target the traditional event type where the initial particles are two gluinos, two squarks or a gluino and a squark³. These then mostly decay into (each other and) either the lightest chargino ($\tilde{\chi}_1^\pm$) or one of the two lightest neutralinos ($\tilde{\chi}_1^0$ and $\tilde{\chi}_2^0$) (since $m_1 < m_2 < \mu$). With a

³They are more model independent exclusion limits for 1- and multi-lepton SUSY channels.

slepton positioned between $\tilde{\chi}_1^\pm / \tilde{\chi}_2^0$ and $\tilde{\chi}_1^0$, the final decay down to $\tilde{\chi}_1^0$ often produces lepton(s). The following parameters are fixed: $m_A = 1000\text{GeV}$, $\mu = 1.5 \times \min(m_{\tilde{g}}, m_{\tilde{q}})$, $\tan \beta = 4$, $A_t = \tan \beta$, $A_b = \tan \beta$, and $A_l = \tan \beta$.

In this signal grid, the masses of third generation sfermions are set to 2 TeV, and common squark and slepton mass parameters are assumed for the first two generations, see possible parameters in Table 2.2. The remaining free parameters are the three gaugino masses and the squark and slepton masses. Two grids in the $(m_{\tilde{g}}, m_{\tilde{q}})$ plane are generated: one yielding soft final state kinematics, defined by $m_{\tilde{\chi}_2^0} = M - 50\text{GeV}$, $m_{\tilde{\chi}_1^0} = M - 150\text{GeV}$ and $m_{\tilde{l}_L} = M - 100\text{GeV}$, where M is the minimum of the gluino and squark mass ("compressed spectrum" models⁴); and one with a very light LSP, yielding a harder spectrum of leptons, jets and \cancel{E}_T , with $m_{\tilde{\chi}_2^0} = M - 100\text{GeV}$, $m_{\tilde{\chi}_1^0} = M - 100\text{GeV}$ and $m_{\tilde{l}_L} = M/2\text{GeV}$ (light neutralino models). SUSY signal events are generated with HERWIG++ for the mSUGRA models and with HERWIG for the MSSM models.

5.3 Electron Identification

Excellent particle identification capability is required at the LHC for most physics studies. There are several channels expected from new physics, for instance some decay modes of the Higgs boson into electrons $H \rightarrow eeee$ or neutralino decays $\tilde{\chi}_2^0 \rightarrow \tilde{\chi}_1^0 + Z^0 \rightarrow \cancel{E}_T + l^+ + l^-$, have small cross-sections and suffer from large (usually QCD) backgrounds. Therefore powerful and efficient electron identification is needed to observe such signals.

Calorimeter isolation is used as a discriminant to separate prompt e/γ objects from non-prompt⁵ electrons and photons as well as jets in many analyses. A photon, γ or electron e^- will leak some of its energy outside the radius of its central cone (calorimeter cells of a certain radius around the γ or e^- cluster barycenter excluding a 5×7 grid of cells in the center of the core) causing the isolation energy to grow as a function of E_T , see Figure 5.3. An ideal isolation variable would include only energy from other objects produced in the hard scatter, but in a real detector, there are other effects that contribute to the energy measured in an isolation cone. These effects include calorimeter noise, lateral leakage of the e/γ object into the isolation cone, and pile-up of events. The primary effect of calorimeter noise is to give the calorimeter isolation distribution a characteristic width.

⁴It is assumed that the MSSM is the effective field theory between M_{weak} and M_{GUT} .

⁵not from the vertex we are interested in, so they may leak to the surrounding calorimeter cells

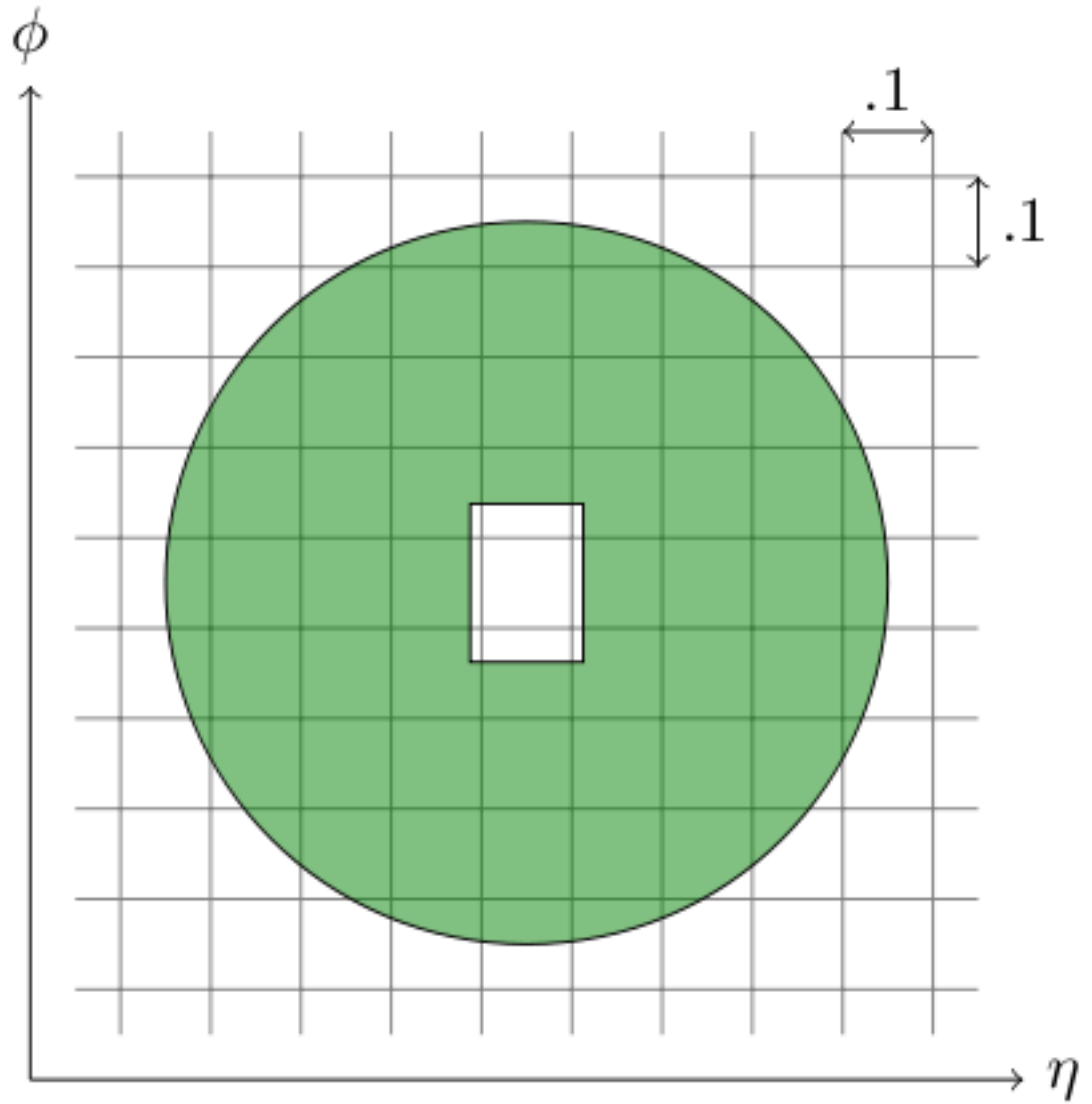


Figure 5.3: A cone size of radius, $\Delta R = 0.4$ is shown here. In the center, there is a grid of cells ignored to reduce the dependence of the Etcone isolation energy on the E_T .

Pileup corrections are temporary and will be improved upon in later AODs. Electrons are required to be isolated and have high transverse momentum since most of them are the decay products of W, and Z bosons. Electron candidates are reconstructed from cluster energy signatures in the EM calorimeter where both electron and photons cascade and deposit their energy with reconstructed tracks pointing back to the ID. There are two kinds of pileup, in-time and out-of-time pileup. For in-time pileup, particles from other interactions in the same bunch crossing leave energy deposits in the calorimeter. Energy increases are observed as they fall into the cone used in the `Etcone` variable. For the out-of-time pileup, there is a delay in the response. The energy time profile of the LAr calorimeter shows a peak and then negative contributions lasting about 600ns. [56]

The ratio between the rates of isolated electrons and the rate of QCD jets with p_T in the range 20-50 GeV is expected to be about 10^{-5} at the LHC [13]. Therefore, to achieve comparable performances, the electron identification capability of the LHC detectors must be almost two orders of magnitude better than what has been achieved so far. A cut selection based on using calorimeters, tracking and combined variables, helps to provide good separation between signal electrons and background from jets that fakes electrons. There are in general three kinds of cuts with varying degrees of selectivity, loose, medium(++ and with track matching) and tight(++ and with track matching).

If we look at the barrel region of the calorimeter, $|\eta| < 2.5$, the loose cuts perform the simplest form of identification based on limited information from the calorimeters. Cuts are applied on the hadronic leakage and shower-shape variables. This set of cuts provides excellent identification efficiency but at the cost of low background rejection [4].

The medium cuts are less efficient than the loose cuts but add quality by rejecting $\pi_0 \rightarrow \gamma\gamma$ decays, insisting on a particular shower shape, at least one hit in the pixel detector and nine in both the pixel and SCT. This is in addition to the criteria for loose cuts. The medium cuts increase the jet rejection by a factor of 3-4 with respect to the loose cuts, while reducing the identification efficiency by 10% [4].

The tight cut is the most restrictive and makes use of all the particle-identification tools currently available for electrons. This is the cut used in this analysis since it provides the lowest fake rates. In addition to the cuts used in the medium set, cuts are applied on the number of vertexing-layer hits (to reject electrons from conversions), on the number of hits in the TRT, on the ratio of high-threshold hits to the number of hits in the TRT (to reject the dominant background from charged hadrons), on the difference between the cluster and the extrapolated track positions in η and ψ , and on the ratio

of cluster energy to track momentum. Two different final selections are available within this tight category: they are named tight (calorimeter isolated) and tight (TRT) and are optimised differently for isolated and non-isolated electrons. In the case of tight (isol) cuts, an additional energy isolation cut is applied to the cluster, using all cell energies within a cone of $\Delta R < 0.2$ around the electron candidate. This set of cuts provides, in general, the highest isolated electron identification and the highest rejection against jets. The tight (TRT) cuts do not include the additional explicit energy isolation cut, but instead apply tighter cuts on the TRT information to further remove the background from charged hadrons [13].

The electron identification in the forward region ($2.5 < |\eta| < 4.9$) is essential in many physics analyses, including electroweak measurements and new phenomena searches. In contrast to the central electron, the forward electron reconstruction uses only the information from the calorimeters as the tracking system is limited to $|\eta| < 2.5$. Obviously it is not possible to distinguish between electrons and photons in the forward region.

The ATLAS e/γ working group recommends the following criteria for electron identification. The use of standard cluster-based algorithms, setting the `author` D3PD variable to 1 or 3. The variable `author` set to 1 means that the object has been found by only the standard (cluster based) algorithm. The variable `author` set to 3 means that the object has been found by the standard (cluster based) and the track-based algorithms⁶. In addition to that, it is recommended to filter for the `EF_e20_medium` true condition, which is a 20GeV electron trigger and also using the electron `medium` variable. Electrons that have absolute pseudorapidity between 1.37 and 1.52 and greater than 2.47 are excluded — `fabs(c1_eta) > 2.47`, `1.37 < fabs(c1_eta) < 1.52`. A transverse energy cut is also applied on the electrons, $E_T > 25\text{GeV}$ which also limits the number of uninteresting electrons with low kinetic energy. The electron track must also not overlap with a muon track to ensure the quality of the electron's track reconstruction. Due to liquid Argon noise bursts in the EM calorimeter, the `OQ` flag must be checked to be true. The electrons should be isolated, as a requirement for QCD background suppression, `etcone20_pt_corrected/e1_c1_et < 0.15`. All these conditions are done using the SUSY group recommended Good Run Lists [44], prepared error free runs suitable for analysis.

⁶Set to 2 means that the object has been found by only the soft (track based) algorithm.

Category	Type of particle	Type of parent particle
Isolated	Electron	Z, W, t, τ or μ
Non-isolated	Electron	J/Ψ , b- or c-hadron decays
Background	Electron	Photon (conversions), π^0/η Dalitz decays, u- d- s-hadron decays
Non-electrons	Charged hadrons, μ	

Table 5.4: Category of simulated electron candidates and their parent particle. Muons are included because they could radiate photons.

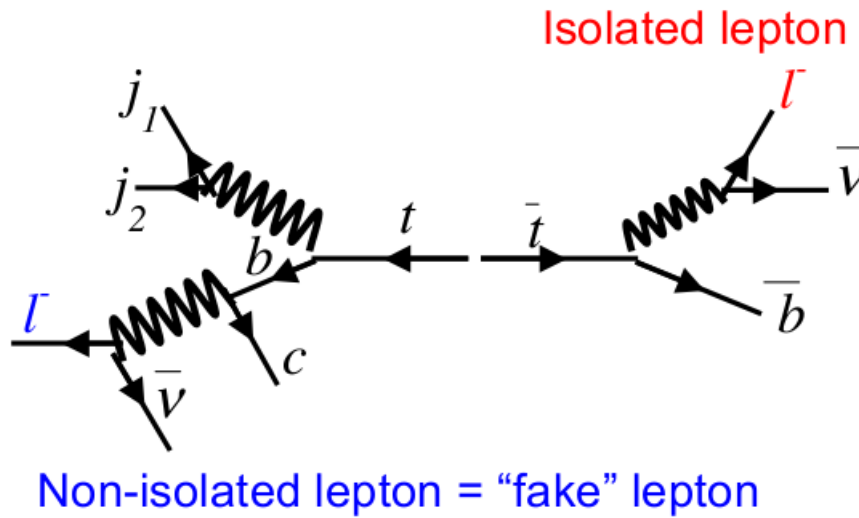


Figure 5.4: An isolated and non-isolated (fake) electron.

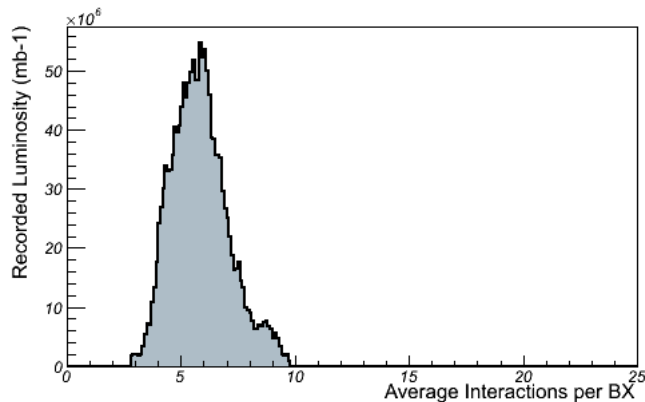


Figure 5.5: Average number of interactions per crossing recorded for period B to K, collected from the beginning of 2011 till mid 2011.

5.4 Systematics, Energy rescaling and Pileup reweightings

Energy rescaling is used to correct electromagnetic cluster energy by applying the energy scales obtained from resonances such as $Z \rightarrow ee$, $J/\psi \rightarrow ee$ or energy/momentum studies using isolated electrons from $W \rightarrow e\nu$ [30] to obtain the right energies that match closer to data.

Monte Carlo samples are produced before or during a given data taking period. By that design, one can only estimate data pileup conditions inserted into the Monte Carlo. Thus, there is the need at the analysis level to reweight the Monte Carlo pileup conditions to what is found in the data taken.

Pileup reweighting [56] is required for MC as of 2011 data taking since the LHC is running with bunch trains with an in-train bunch separation of 50ns. The out-of-time pileup is very important as the number of vertices in a given event is not a good measure any more as compared to 2010 data. Instead, one needs to use in most analysis cases the average number of pileup interactions $\langle \mu \rangle$. μ is a measure of how many proton-proton collisions are expected per event. Figure 5.5 shows the average interaction per crossing, or $\langle \mu \rangle$ which is directly correlated to the instantaneous luminosity and is used to calculate and reweight pileup in MC. Figure 5.6 shows the delivered luminosity to the ATLAS detector.

Since the MC dataset does not reproduce the resolution in data, a smearing procedure can be applied to the MC dataset. The method takes pseudorapidity, energy and a constant error term as arguments and returns the

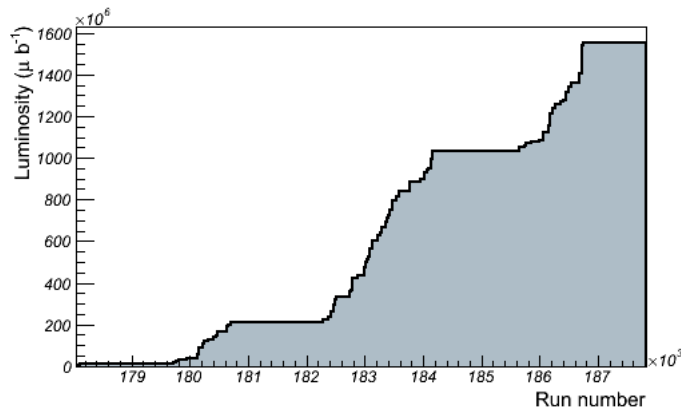


Figure 5.6: ATLAS recorded luminosity.

smearing correction. An efficiency scale factor, in Equation 5.1 is applied to MC and it describes all reconstruction, identification and trigger efficiencies to match data efficiencies.

$$SF(\eta, p_T) = \frac{\epsilon_{DATA}(\eta, p_T)}{\epsilon_{MC}(\eta, p_T)} \quad (5.1)$$

The systematic error for luminosity is 3.7% [6]. Primary sources of uncertainty are from the jet energy scale (JES) estimated to be about 11%, jet energy resolution (JER) about 1% [5], initial/final state radiation (ISR/FSR) about 27%, MC generator about 16% for $t\bar{t}$ events [38].

5.5 Dielectron channel studies

Data recorded from the LHC by the ATLAS detector run period B to period K, also shown in Figure 5.6 from early to mid-2011 is used for the study. We then proceed to use the luminosity to normalize MC datasets. Each of the MC processes have NLO cross sections and event numbers, refer back to Table 5.2. In the following plots, Figures 5.7 and 5.8 show the invariant mass data plots and their deviations from MC predictions. Invariant mass is defined to be $m_{inv} = \sqrt{(E_1 + E_2)^2 + (\vec{p}_1 + \vec{p}_2)^2}$ for dielectrons. Most heavy particles decay into a lepton-antilepton pair such as the Z -boson and the J/ψ . They trace out a Breit-Wigner peak in these histograms, which is useful to study particle mass and lifetime.

It is possible to reduce the Drell-Yan background by imposing an extra missing transverse energy cut, $\cancel{E}_T > 100\text{GeV}$. Since the Z boson decay produces low \cancel{E}_T , this kinematic cut will reject these events. As a comparison, the $\tilde{\chi}_2^0$ have higher \cancel{E}_T . The plots in Figures 5.7 show the distribution of dielectron invariant mass with a distinct Z mass peak. The SM Monte Carlo background explains the data well with no hint of any new physics. mSUGRA and PhenoGrid suggest that if there is supersymmetry, there will be a mass edge at the low mass region between 40-100GeV, although at current luminosities, there are barely enough expected SUSY events to register an edge. Even with a $\cancel{E}_T > 100\text{ GeV}$ cut in Figure 5.8, there is no significant deviation from SM.

Two jets and two lepton events can be from gluino decays into the $\tilde{\chi}_2^0$ pair decays so by applying a jet multiplicity cut, to pass events that have at least one jet would also decrease much of the SM background. The results are shown in the jet multiplicity plot in 5.9 and 5.10; they agree well with SM predictions. The SUSY signals are still below the levels required to see them. More events are possible with the MSSM24, but the mass edge does appear to overlap with the Z resonance peak which is quite a problem.

Top-antitop quark pairs are produced in LHC mostly through the process $gg \rightarrow t\bar{t}$ (87%) and the rest through quark-antiquark annihilation. The top spin correlations have been studied since CDF and D0 [10], [40], [7]. It is interesting to study the top spin correlations because they can be different from the SM if the $t\bar{t}$ is produced by the exchange of a virtual heavy Higgs boson [17] or if the top quark decays into a charged Higgs boson and a b-quark [41] and it is the closest we can get to studying bare quarks. Here, we show how SUSY particles like the $\tilde{\chi}_2^0$ could differ from the $t\bar{t}$ spin correlation in Figure 5.11.

The decay lifetime of the top quark, $\Gamma_t \approx 1.5\text{GeV}$, which is much larger than the typical hadronization scale, $\Lambda_{QCD} \approx 0.2\text{GeV}$. So the top quark decays weakly before being hadronized. It is then possible to obtain the spin information of the top quark. Electrons from the top weak decays can be used to study the decay process.

The spins could become decorrelated if the spins of the top quarks flip before they decay. Figure 5.12 shows the plot for the azimuthal angle distribution, $\Delta\phi$ of the electron pairs produced with MET of at least 100GeV to cut away the Z boson decay events. The azimuthal angle, ϕ is studied since it is well measured in the ATLAS detector, and does not require the reconstruction of the top quark.

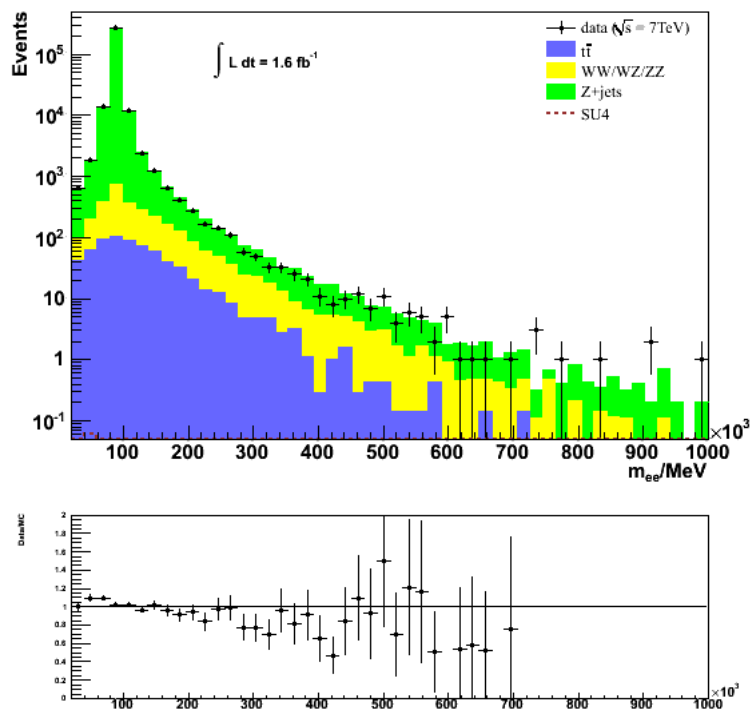


Figure 5.7: Dielectron invariant mass.

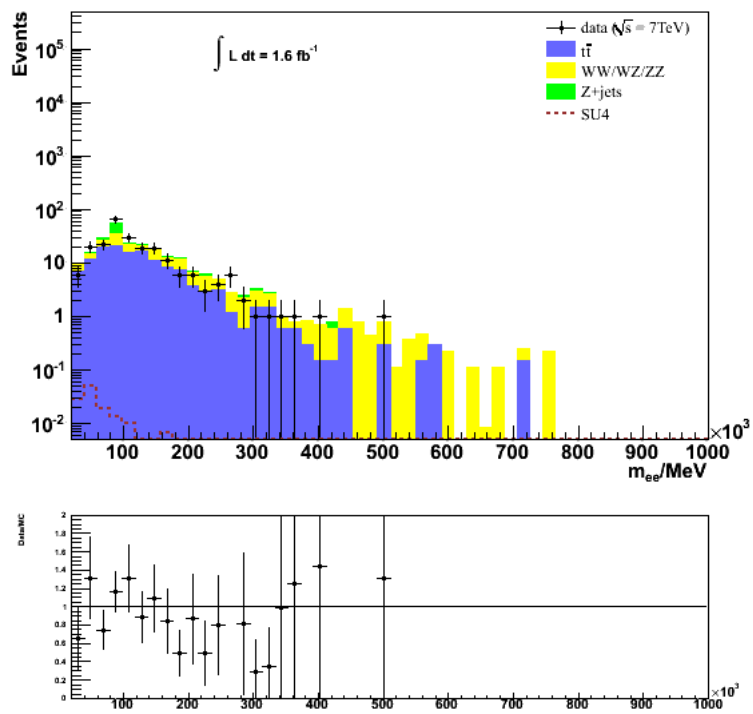


Figure 5.8: Dielectron invariant mass with missing $\cancel{E}_T > 100$ GeV.

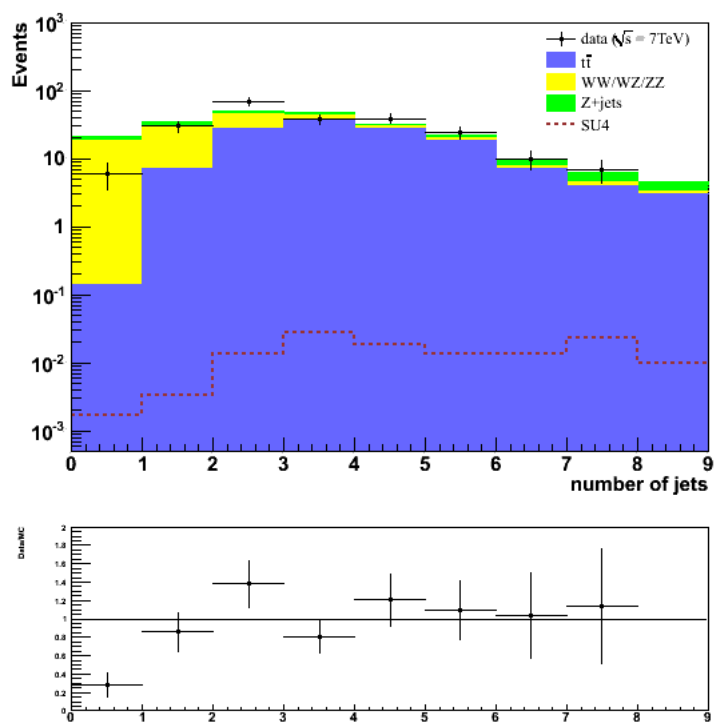


Figure 5.9: Number of jets with a $\cancel{E}_T > 100$ GeV cut. Note that $t\bar{t}$ events dominate. The red dotted lines show the SUSY SU4 signal.

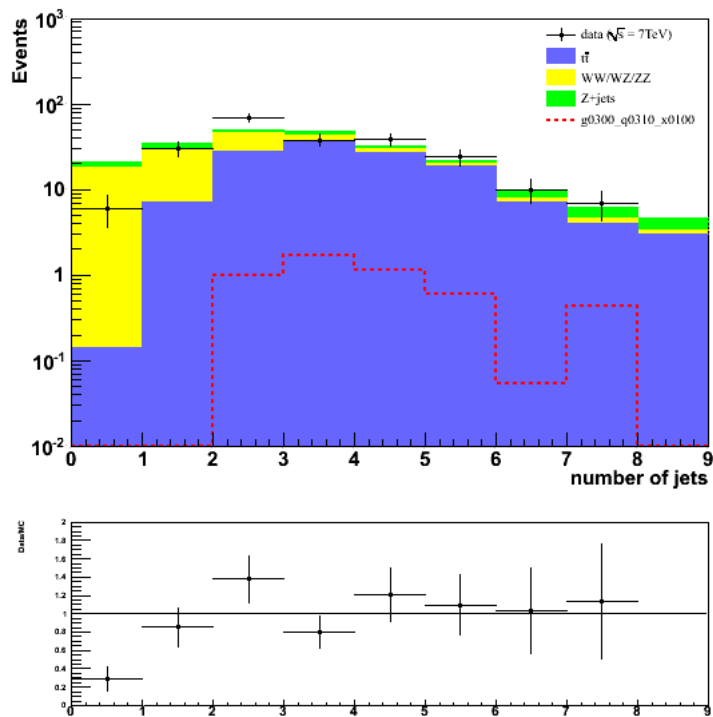


Figure 5.10: Similar to Figure 5.9, but now with SUSY MSSM24 signal, with parameters gluino mass: 300GeV, squark mass: 310GeV, LSP mass: 100GeV.

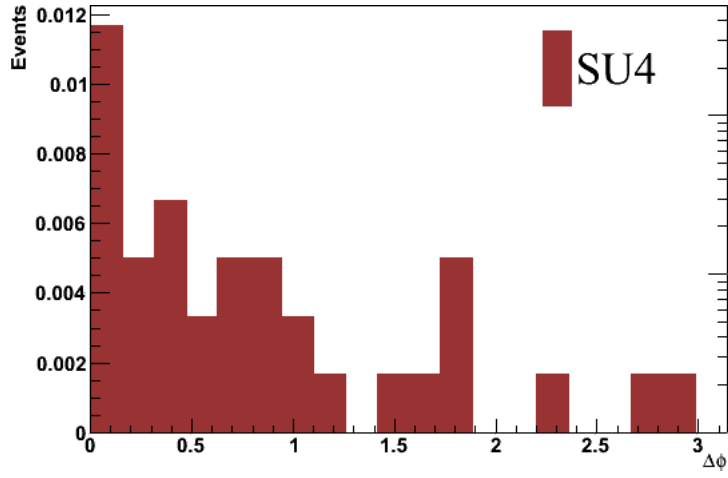


Figure 5.11: The ϕ angle difference between the electron-positron pair produced from $\tilde{\chi}_2^0$ decay.

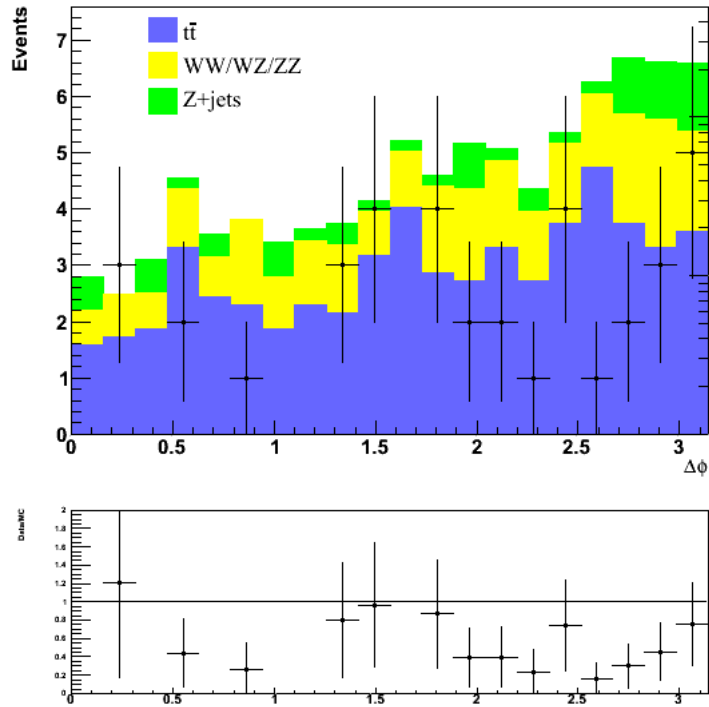


Figure 5.12: Dielectron azimuthal angle difference with missing $\cancel{E}_T > 100$ GeV.

5.6 Sliding q_T Ratio Method

The method described in the previous section employs all available means to suppress SM background which usually also takes away interesting signals that may be BSM signals. This is done by filtering events with $\cancel{E}_T < 100$ GeV. This comes with the risk of reducing the available data to very little statistics to actually conclude anything. The Sliding q_T ratio method [57] does not attempt to reduce the SM background but instead assumes that near the Z mass peak, the SM background dominates all and uses the invariant mass range 85 - 100 GeV as normalization.

Consider the signal to be from the decay of the second lightest neutralino, $\tilde{\chi}_2^0$ into dilepton pairs and $\tilde{\chi}_1^0$ which is \cancel{E}_T . This would appear as moderately high m_{ll} and large dielectron transverse momentum, q_T . The high q_T comes from the mass of the three-body nature of the decay with the $\tilde{\chi}_1^0$ being ignored for this search.

The main source of background would be the Drell-Yan process including the Z resonance, but they should have small q_T , unless they are boosted, as it is shown in Figure 5.15. Other q_T plots are shown in Figures 5.13, 5.14, 5.16 and 5.17. There are of course other SM processes like $t\bar{t}$ and diboson decays that cannot be distinguished by just looking at the final state lepton pairs but at Z resonance region, they are negligible.

Here we start with opposite sign same-flavour dielectrons for invariant mass, $m_{ee} > 20\text{GeV}$. A leading electron with $p_T > 20\text{GeV}$ and a sub-leading electron with $p_T > 10\text{GeV}$ both with tight identification cuts. The sample is then divided into five regions,

$$\begin{aligned}
 \text{Region 1: } & 25 < m_{ee} < 65\text{GeV} \\
 \text{Region 2: } & 65 < m_{ee} < 85\text{GeV} \\
 \text{Region 3: } & 85 < m_{ee} < 100\text{GeV} \\
 \text{Region 4: } & 100 < m_{ee} < 120\text{GeV} \\
 \text{Region 5: } & m_{ee} > 120\text{GeV}
 \end{aligned}
 \tag{5.2}$$

Region 3 is dominated by the SM Z boson resonance which is well known as it has been studied since the LEP and Tevatron days. In this analysis, this region will be used as a benchmark to normalize the data and monte carlo. We take the ratios of event yields in regions 1, 2, 4 and 5 to region 3 and call them F_1 , F_2 , F_4 , and F_5 . $\tilde{\chi}_2^0$ production would primarily contribute to region 1 so if there is a signal there would be a bump in this region. However, the Drell-Yan background is still very significant and hides this neutralino signal from being easily seen.

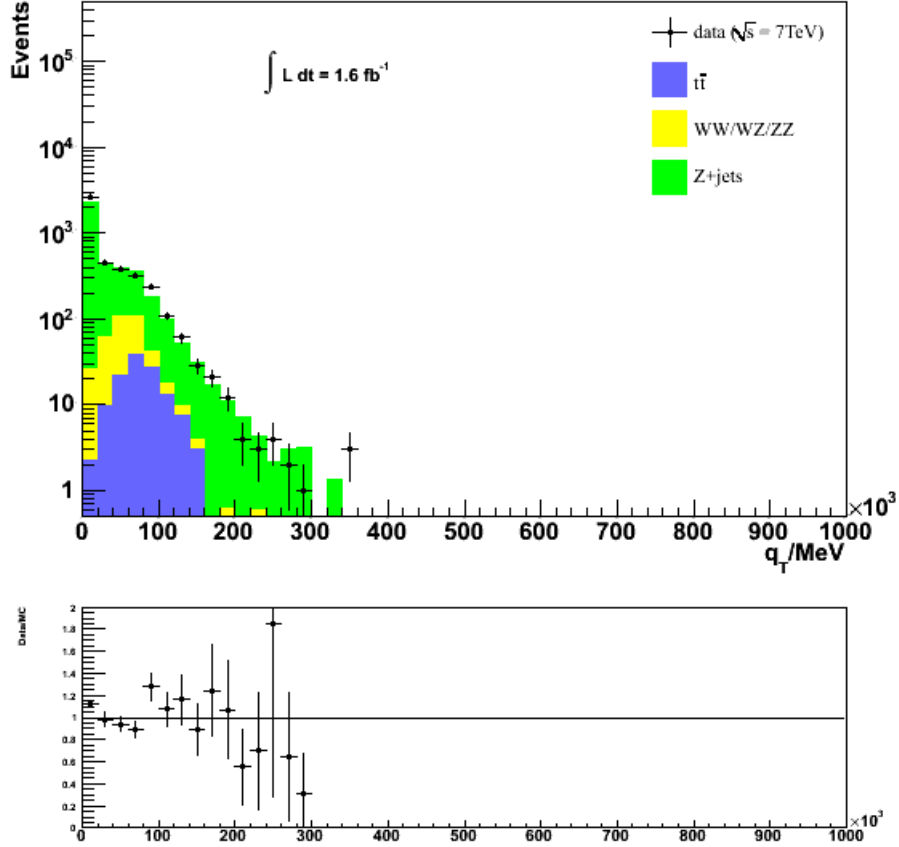


Figure 5.13: q_T for opposite sign invariant mass between 25 GeV and 65 GeV.

Therefore we require something to reduce the Drell-Yan background as it is known that Drell-Yan processes have low q_T so if we introduce a q_T cut, the Drell-Yan events could be removed. The sliding ratio is demonstrated in Figure 5.23. The plots show the ratios, $F_i (i = 1, 2, 4, 5)$ agree well with SM predictions. Figure 5.24 shows SUSY SU4 neutralino ratio profile. Note that there is a distinct bump peaking at $\min q_T \approx 50 \text{ GeV}$ and a dip near the Z mass for ratio F_1 . So one can say that there is not enough statistics to see any neutralino or BSM in the current data recorded.

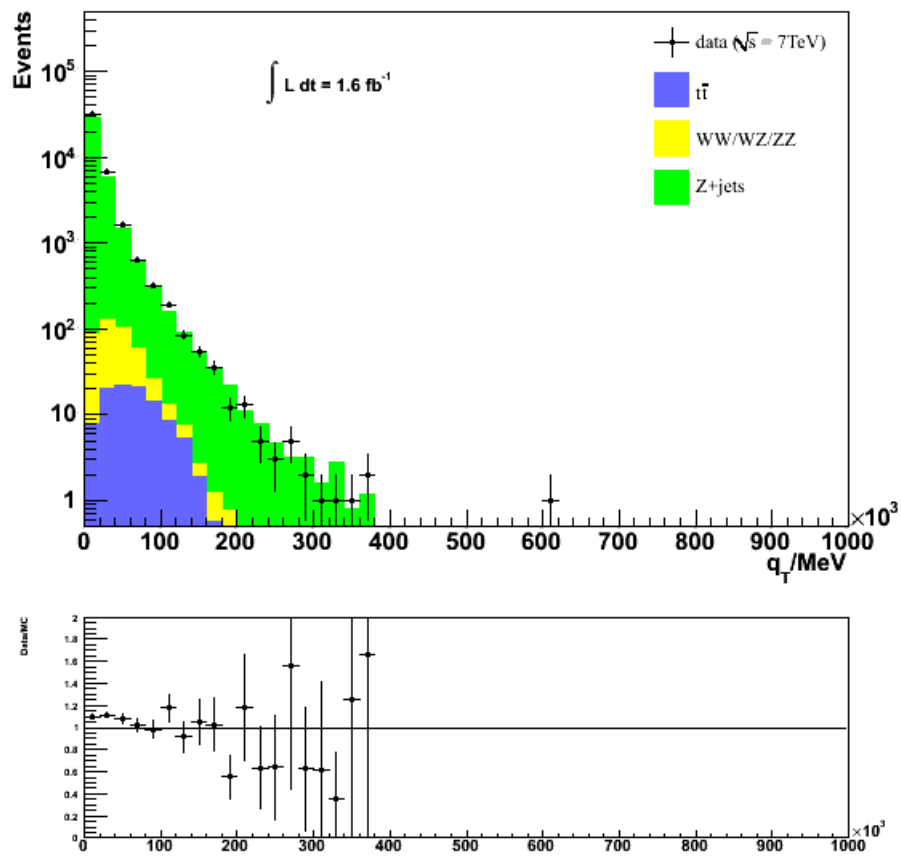


Figure 5.14: q_T for opposite sign invariant mass between 65 GeV and 85 GeV.

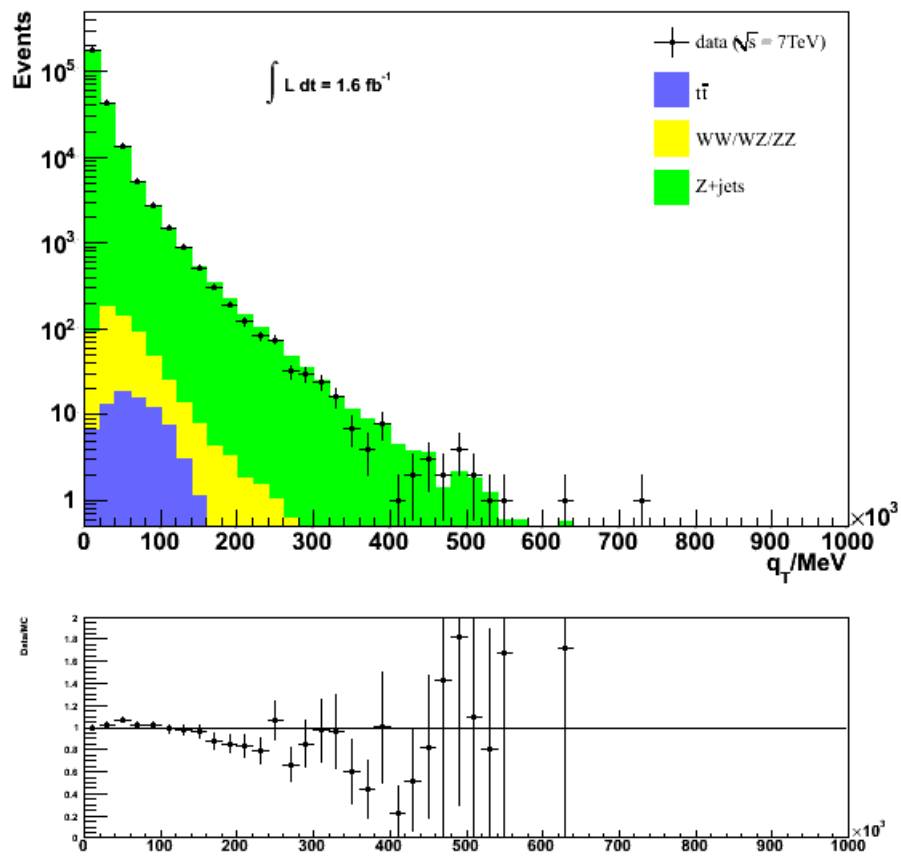


Figure 5.15: q_T for opposite sign invariant mass between 85GeV and 100GeV.

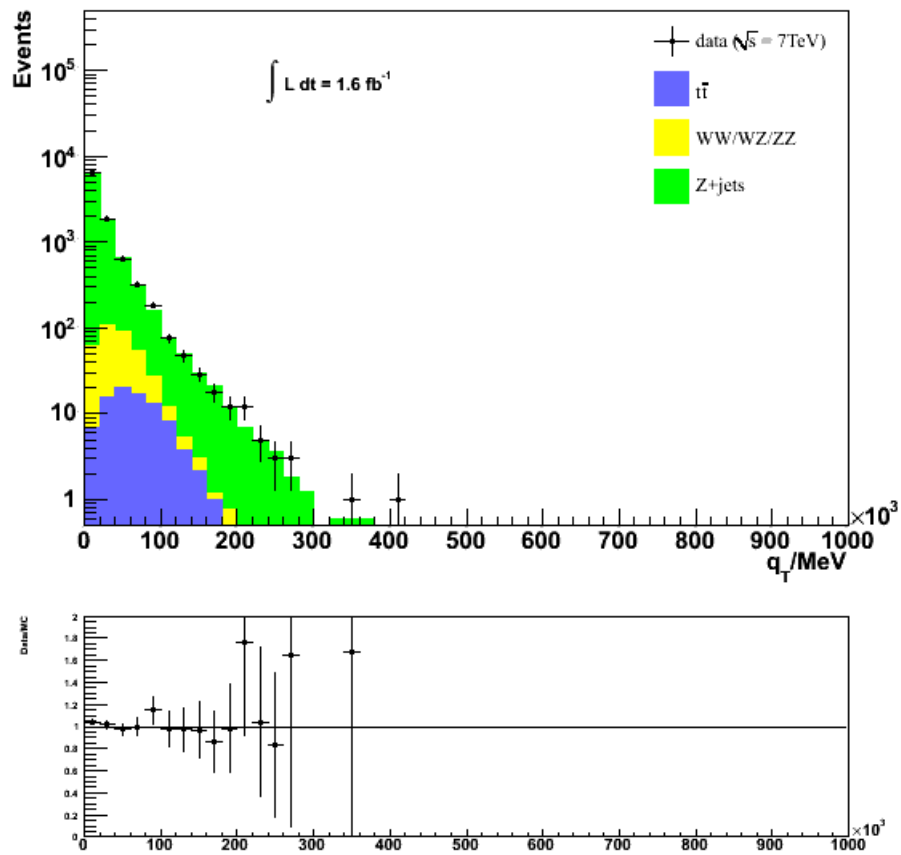


Figure 5.16: q_T for opposite sign invariant mass between 100GeV and 120GeV.

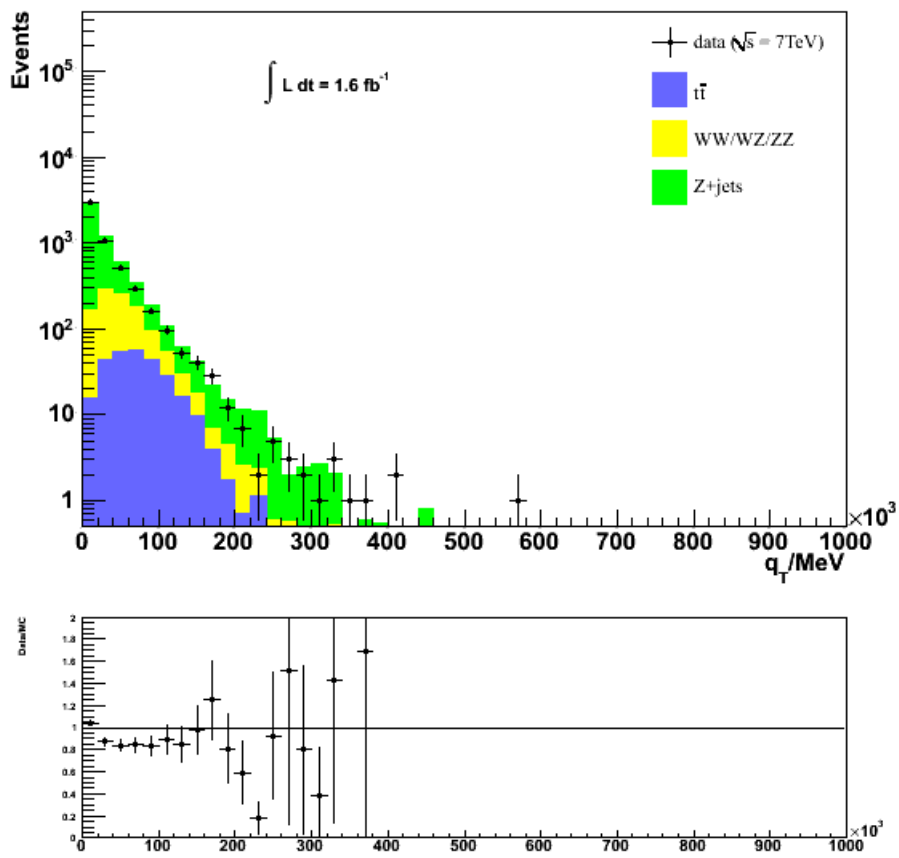


Figure 5.17: q_T for opposite sign invariant mass more than 120 GeV.

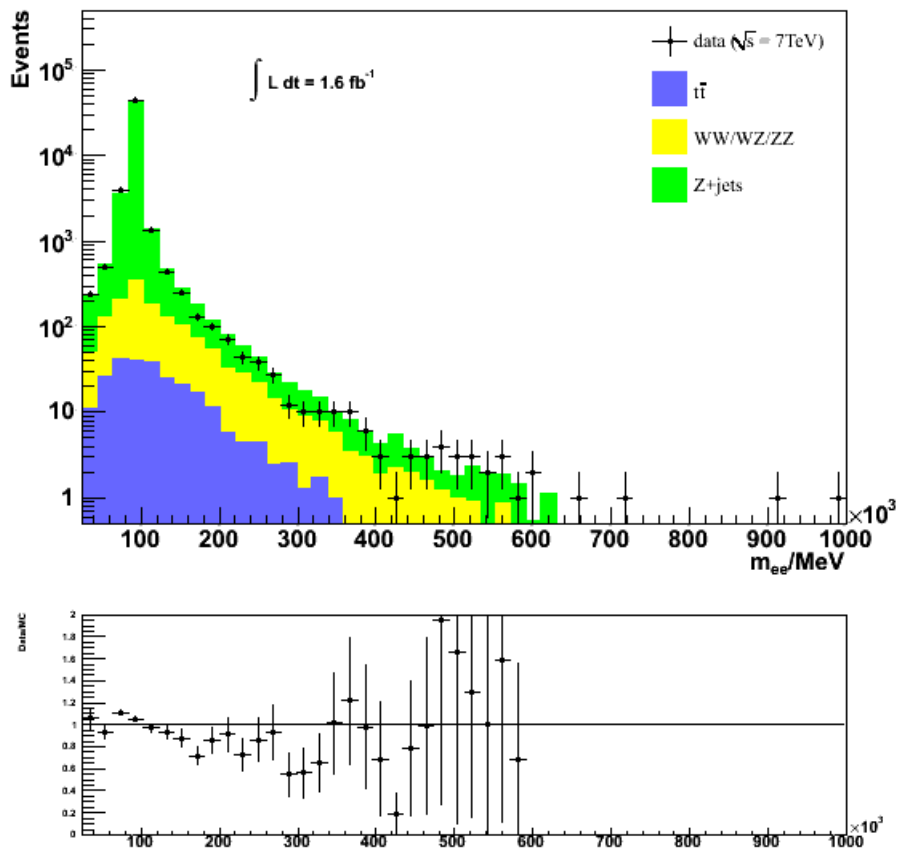


Figure 5.18: m_{ee} for q_T between 25GeV and 65GeV.

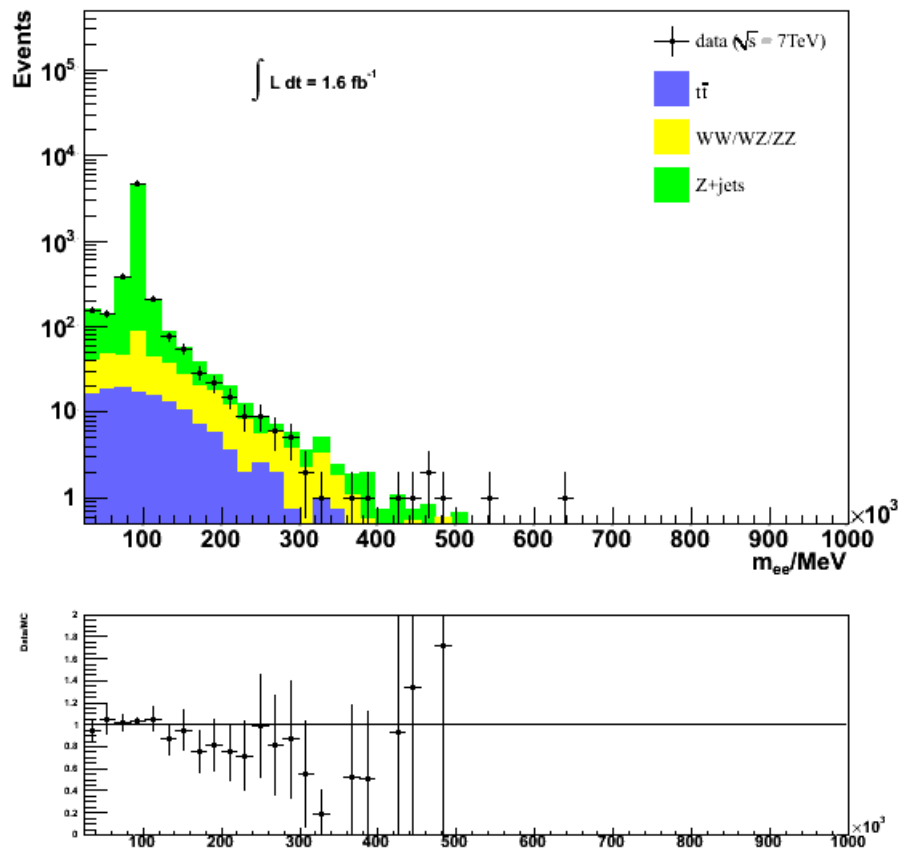


Figure 5.19: m_{ee} for q_T between 65GeV and 85GeV.

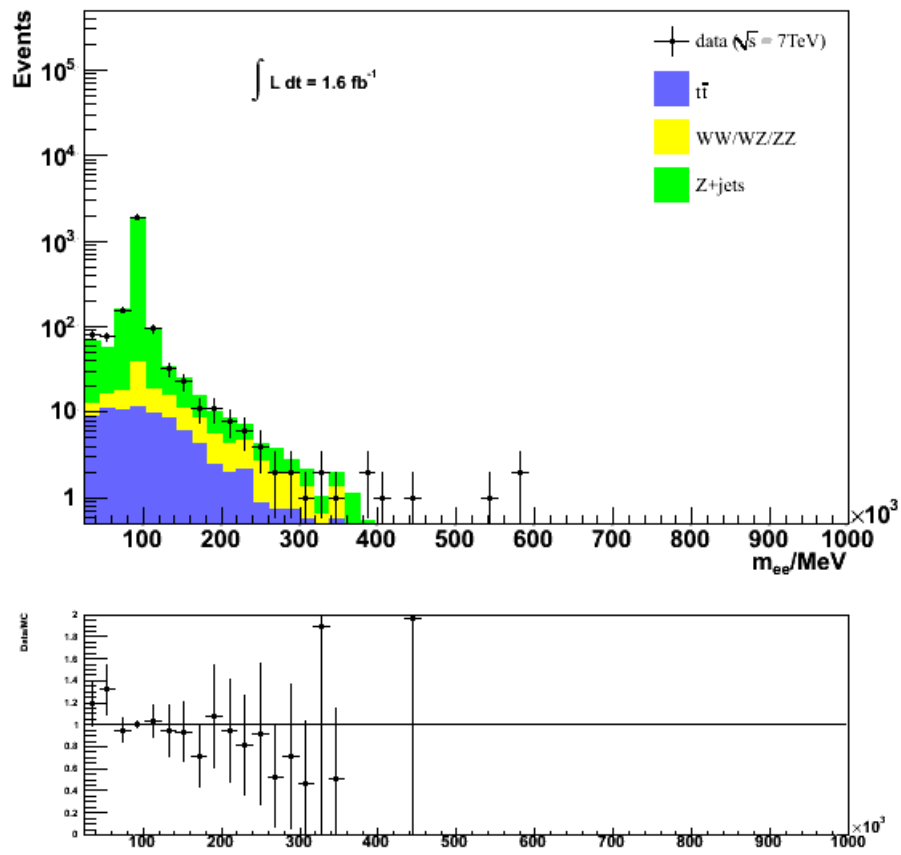


Figure 5.20: m_{ee} for q_T between 85GeV and 100GeV.

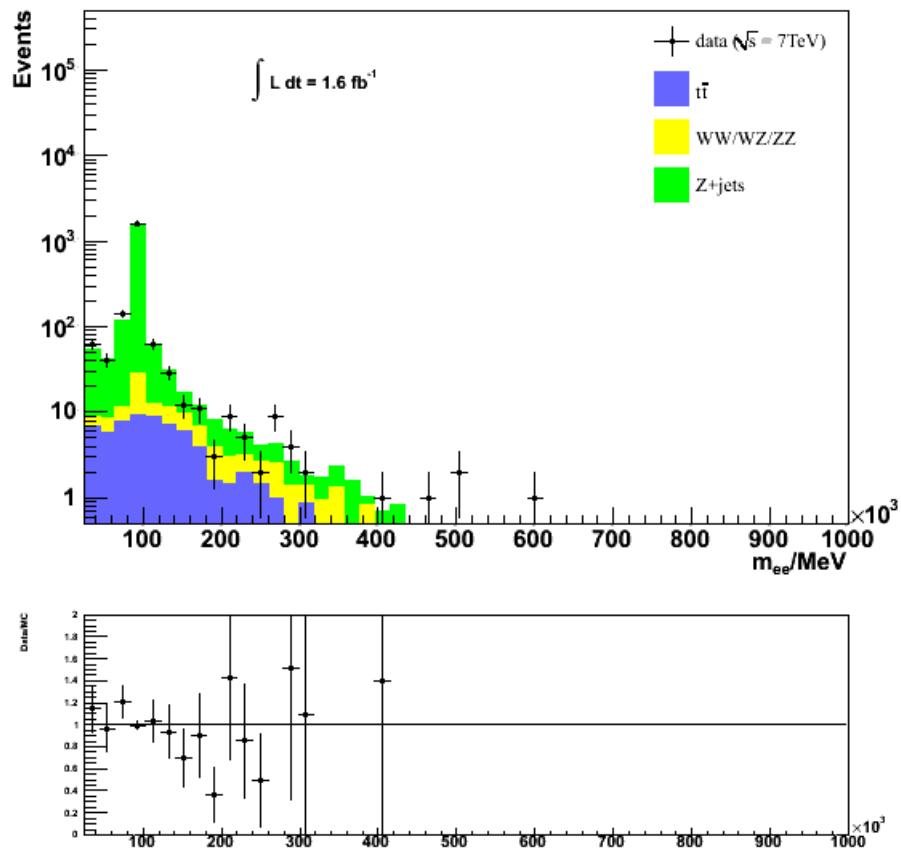


Figure 5.21: m_{ee} for q_T between 100GeV and 120GeV.

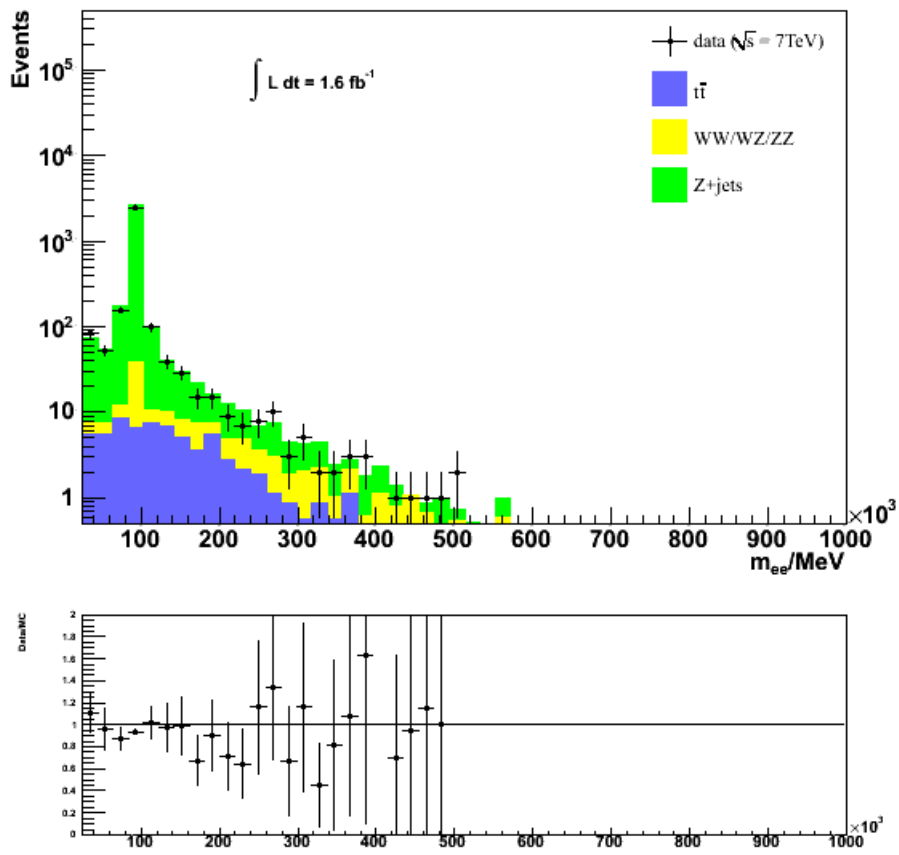


Figure 5.22: m_{ee} for $q_T > 120\text{GeV}$.

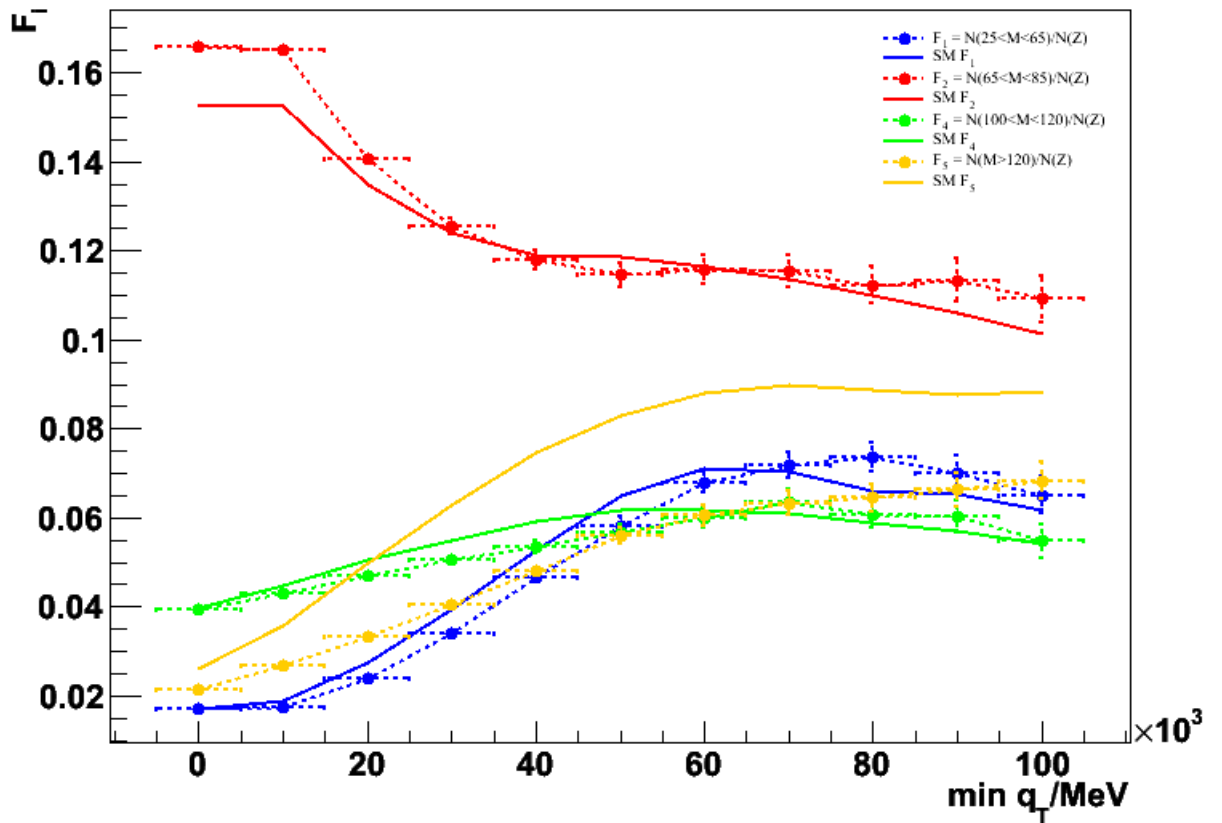


Figure 5.23: MC and data ratios, F_i ($i = 1, 2, 4, 5$). Blue is F_1 , red is F_2 , green is F_4 and yellow is F_5 . Solid points with error bars and dotted lines are data points. Solid lines are SM MC predictions. F_i ($i = 1, 2, 4$) show no significant deviation away from SM, but F_5 does. It is mainly due to low statistics at high invariant mass and high momentum.

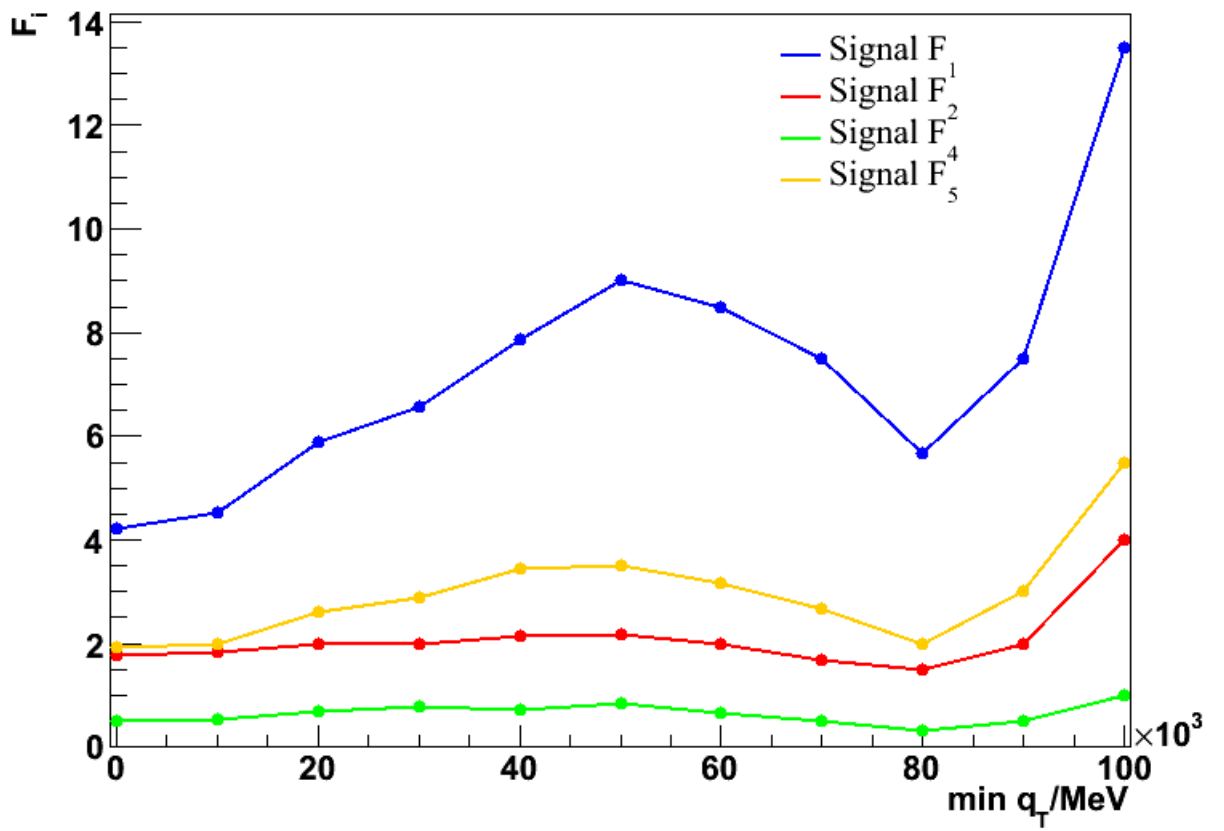


Figure 5.24: Proof of principle. MC generated SUSY SU4 signal ratios which do show a bump at the expected momentum.

Chapter 6

Conclusion

We study data recorded by ATLAS from the LHC proton-proton collisions at $\sqrt{s} = 7\text{TeV}$ between early to mid 2011, producing in total about 1.6fb^{-1} of events. SUSY models such as the mSUGRA and the MSSM24 have been studied using dielectrons. In particular we analyse the decay chain $\tilde{q}_L \rightarrow \tilde{\chi}_2^0 q \rightarrow \tilde{l}_{L,R}^\pm l^\mp q \rightarrow l^+ l^- q \tilde{\chi}_1^0$ in the opposite sign dielectron channel.

However, there is not enough luminosity for SUSY particles to appear as it is calculated that if mSUGRA is valid, it would need at least 10fb^{-1} worth of events to see the first SUSY events appearing.

I also showed the methods of optimizing data processing in the grid. Instead of manual and serially submitting job requests, a python script is used for parallel submission and error management both in Panda and Nordugrid. This provides a convenient way of processing data over the grid as it is quite time consuming to organize job specifications and making sure they are run properly.

Various analysis methods are used to study the invariant mass of dielectrons using MET cuts and also the Sliding q_T method which has not been applied using ATLAS data. Analysis shows that both are in agreement with the SM. There is not enough statistics to say anything much about the high energy tail in the invariant mass spectrum, as there is too much statistical errors present.

Perhaps in the future with increasing luminosity and center of mass collision energy, new physics will start to appear in the LHC and be found by the ATLAS detector.

Nomenclature

ALICE A Large Ion Collider Experiment

AOD Analysis Object Data

ATLAS A Toroidal LHC ApparatuS

AtlFast ATLAS Fast

BSM Beyond the Standard Model

CA Certificate Authorities

CMS Compact Muon Solenoid

ECal Electromagnetic Calorimeter

GEANT4 GEometry ANd Tracking

GM Grid Manager

GMSB Gauge Mediated Symmetry Breaking

GUT Grand Unified Theory

HCal Hadronic Calorimeter

ID Inner Detector

JER Jet Energy Resolution

JES Jet Energy Scale

L1 Level 1 Trigger

L2 Level 2 Trigger

LAr Liquid Argon

LHCb LHC beauty
LRMS Local Resource Management System
LSP Lightest Supersymmetric Particle
MC Monte Carlo
MET Missing transverse energy
MSSM Minimal Supersymmetric Standard Model
mSUGRA minimal Super GRAvity
NLO next to leading order
NNLO next-to-next to leading order
QCD Quantum Chromodynamics
SCT Semiconductor Tracker
SM Standard Model
SUSY Supersymmetry
TRT Transition Radiation Tracker
VO Virtual Organizations
WLCG Worldwide LHC Computing Grid
XRSL Extended Resource Specification Language

Appendix A

SM D3PD

mc10_7TeV.107680.AlpgeJimmyWenuNp0_pt20.merge.NTUP_SUSY.e600_s933_s946_r2302_r2300_p601
mc10_7TeV.107681.AlpgeJimmyWenuNp1_pt20.merge.NTUP_SUSY.e600_s933_s946_r2302_r2300_p601
mc10_7TeV.107682.AlpgeJimmyWenuNp2_pt20.merge.NTUP_SUSY.e760_s933_s946_r2302_r2300_p601
mc10_7TeV.107683.AlpgeJimmyWenuNp3_pt20.merge.NTUP_SUSY.e760_s933_s946_r2302_r2300_p601
mc10_7TeV.107684.AlpgeJimmyWenuNp4_pt20.merge.NTUP_SUSY.e760_s933_s946_r2302_r2300_p601
mc10_7TeV.107685.AlpgeJimmyWenuNp5_pt20.merge.NTUP_SUSY.e760_s933_s946_r2302_r2300_p601
mc10_7TeV.107650.AlpgeJimmyZeeNp0_pt20.merge.NTUP_SUSY.e737_s933_s946_r2302_r2300_p601
mc10_7TeV.107651.AlpgeJimmyZeeNp1_pt20.merge.NTUP_SUSY.e737_s933_s946_r2302_r2300_p601
mc10_7TeV.107652.AlpgeJimmyZeeNp2_pt20.merge.NTUP_SUSY.e737_s933_s946_r2302_r2300_p601
mc10_7TeV.107653.AlpgeJimmyZeeNp3_pt20.merge.NTUP_SUSY.e737_s933_s946_r2302_r2300_p601
mc10_7TeV.107654.AlpgeJimmyZeeNp4_pt20.merge.NTUP_SUSY.e737_s933_s946_r2302_r2300_p601
mc10_7TeV.107655.AlpgeJimmyZeeNp5_pt20.merge.NTUP_SUSY.e737_s933_s946_r2302_r2300_p601
mc10_7TeV.116250.AlpgeJimmyZeeNp0_Mll110to40_pt20.merge.NTUP_SUSY.e660_s933_s946_r2302_r2300_p601
mc10_7TeV.116251.AlpgeJimmyZeeNp1_Mll110to40_pt20.merge.NTUP_SUSY.e660_s933_s946_r2302_r2300_p601
mc10_7TeV.116252.AlpgeJimmyZeeNp2_Mll110to40_pt20.merge.NTUP_SUSY.e660_s933_s946_r2302_r2300_p601
mc10_7TeV.116253.AlpgeJimmyZeeNp3_Mll110to40_pt20.merge.NTUP_SUSY.e660_s933_s946_r2302_r2300_p601
mc10_7TeV.116254.AlpgeJimmyZeeNp4_Mll110to40_pt20.merge.NTUP_SUSY.e660_s933_s946_r2302_r2300_p601
mc10_7TeV.116255.AlpgeJimmyZeeNp5_Mll110to40_pt20.merge.NTUP_SUSY.e660_s933_s946_r2302_r2300_p601
mc10_7TeV.105861.TTbar_PowHeg_Pythia.merge.NTUP_SUSY.e686_s933_s946_r2302_r2300_p601
mc10_7TeV.105985.WW_Herwig.merge.NTUP_SUSY.e598_s933_s946_r2302_r2300_p601
mc10_7TeV.105986.ZZ_Herwig.merge.NTUP_SUSY.e598_s933_s946_r2302_r2300_p601
mc10_7TeV.105987.WZ_Herwig.merge.NTUP_SUSY.e598_s933_s946_r2302_r2300_p601

Bibliography

- [1] *ATLAS level-1 trigger: Technical Design Report*. Technical Design Report ATLAS. CERN, Geneva, 1998.
- [2] *ATLAS detector and physics performance: Technical Design Report, 1*. Technical Design Report ATLAS. CERN, Geneva, 1999. Electronic version not available.
- [3] Susy chapter. Technical Report ATL-PHYS-PUB-2008-06, CERN, Geneva, Aug 2008. CSC PUB Note.
- [4] Reconstruction and identification of electrons. Technical Report ATL-PHYS-PUB-2009-004. ATL-COM-PHYS-2009-170, CERN, Geneva, Apr 2009. CSC PUB Note.
- [5] Jet energy scale and its systematic uncertainty for jets produced in proton-proton collisions at $\sqrt{s} = 7$ tev and measured with the atlas detector. Technical Report ATLAS-CONF-2010-056, CERN, Geneva, Jul 2010.
- [6] Updated luminosity determination in pp collisions at $\sqrt{s}=7$ tev using the atlas detector. Technical Report ATLAS-CONF-2011-011, CERN, Geneva, Mar 2011.
- [7] S. Abachi. Observation of the top quark. 1995.
- [8] Shehu S. AbdusSalam. The Full 24-Parameter MSSM Exploration. *AIP Conf. Proc.*, 1078:297–299, 2009.
- [9] S. Agostinelli et al. GEANT4: A simulation toolkit. *Nucl. Instrum. Meth.*, A506:250–303, 2003.
- [10] V Abazov et al. Measurement of spin correlation in ttbar production using dilepton final states. Technical Report arXiv:1103.1871. FERMILAB-PUB-11-052-E, Mar 2011. Comments: 10 pages, 3 figures, submitted to PLB.

- [11] Simone Alioli, Paolo Nason, Carlo Oleari, and Emanuele Re. A general framework for implementing NLO calculations in shower Monte Carlo programs: the POWHEG BOX. *JHEP*, 1006:043, 2010.
- [12] B. Andersson, G. Gustafson, G. Ingelman, and T. Sjöstrand. Parton fragmentation and string dynamics. *Physics Reports*, 97(2-3):31 – 145, 1983.
- [13] O Arnaez. Electron reconstruction and identification with the atlas detector. Technical Report ATL-PHYS-PROC-2009-118, CERN, Geneva, Oct 2009.
- [14] Howard Baer, P. G. Mercadante, Xerxes Tata, and Yili Wang. Reach of the cern large hadron collider for gauge-mediated supersymmetry breaking models. *Phys. Rev. D*, 62:095007, Oct 2000.
- [15] W. Beenakker, R. Hopker, and M. Spira. PROSPINO: A program for the PROduction of Supersymmetric Particles In Next-to-leading Order QCD. 1996.
- [16] Krzysztof Benedyczak, Piotr Bala, Sven van den Berghe, Roger Menday, and Bernd Schuller. Key aspects of the unicore 6 security model. *Future Generation Comp. Syst.*, 27(2):195–201, 2011.
- [17] W. Bernreuther, M. Flesch, and P. Haberl. Signatures of higgs bosons in the top quark decay channel at hadron colliders. *Phys. Rev. D*, 58:114031, Nov 1998.
- [18] John M. Brooke and Michael S. Parkin. Enabling scientific collaboration on the grid. *Future Generation Computer Systems*, 26(3):521 – 530, 2010.
- [19] Oliver Sim Brüning, Paul Collier, P Lebrun, Stephen Myers, Ranko Ostojic, John Poole, and Paul Proudlock. *LHC Design Report*. CERN, Geneva, 2004.
- [20] J Butterworth, E Dobson, U Klein, B Mellado Garcia, T Nunnemann, J Qian, D Rebuzzi, and R Tanaka. Single boson and diboson production cross sections in pp collisions at $\sqrt{s}=7$ tev. Technical Report ATL-COM-PHYS-2010-695, CERN, Geneva, Aug 2010.
- [21] J. M. Butterworth, Jeffrey R. Forshaw, and M. H. Seymour. Multiparton interactions in photoproduction at HERA. *Z. Phys.*, C72:637–646, 1996.

- [22] Matteo Cacciari, Gavin P. Salam, and Gregory Soyez. The anti- k_t jet clustering algorithm. *Journal of High Energy Physics*, 2008(04):063, 2008.
- [23] Ben Cerio. Inclusive search for same-sign dileptons at atlas. Technical Report arXiv:1109.5646. ATL-PHYS-PROC-2011-126, CERN, Geneva, Sep 2011.
- [24] A. H. Chamseddine, R. Arnowitt, and Pran Nath. Locally supersymmetric grand unification. *Phys. Rev. Lett.*, 49:970–974, Oct 1982.
- [25] D.J.H. Chung, L.L. Everett, G.L. Kane, S.F. King, J. Lykken, and Lian-Tao Wang. The soft supersymmetry-breaking lagrangian: theory and applications. *Physics Reports*, 407(1-3):1 – 203, 2005.
- [26] ATLAS Collaboration. Atlas tracking event data model. Technical Report ATL-SOFT-PUB-2006-004, CERN, Geneva, 2006.
- [27] ATLAS Collaboration. Expected Performance of the ATLAS Experiment - Detector, Trigger and Physics. 2009.
- [28] ATLAS Collaboration. First tuning of herwig/jimmy to atlas data. Technical Report ATL-PHYS-PUB-2010-014, CERN, Geneva, Oct 2010.
- [29] ATLAS Collaboration. Atlas collaboration website, www.atlas.ch, 2011.
- [30] ATLAS Collaboration. Electron performance measurements with the atlas detector using the 2010 lhc proton-proton collision data. Technical Report arXiv:1110.3174. CERN-PH-EP-2011-117, CERN, Geneva, Oct 2011.
- [31] ATLAS Collaboration. Inclusive search for same-sign dilepton signatures in pp collisions at $\sqrt{s} = 7$ TeV with the ATLAS detector. 2011.
- [32] ATLAS Collaboration. Search for a heavy gauge boson decaying to a charged lepton and a neutrino in 1 fb^{-1} of pp collisions at $\sqrt{s} = 7$ TeV using the ATLAS detector. 2011.
- [33] ATLAS Collaboration. Search for a heavy Standard Model Higgs boson in the channel $H \rightarrow ZZ \rightarrow llqq$ using the ATLAS detector. 2011.
- [34] ATLAS Collaboration. Search for dilepton resonances in pp collisions at $\sqrt{s} = 7$ TeV with the ATLAS detector. 2011.

- [35] ATLAS Collaboration. Search for New Physics in the Dijet Mass Distribution using 1 fb^{-1} of pp Collision Data at $\sqrt{s} = 7 \text{ TeV}$ collected by the ATLAS Detector. 2011.
- [36] ATLAS Collaboration. Search for supersymmetry in final states with jets, missing transverse momentum and one isolated lepton in $\sqrt{s} = 7 \text{ TeV}$ pp collisions using 1 fb^{-1} of ATLAS data. 2011.
- [37] ATLAS Collaboration. Search for the Standard Model Higgs boson in the two photon decay channel with the ATLAS detector at the LHC. 2011.
- [38] Atlas Collaboration. Searches for supersymmetry with the atlas detector using final states with two leptons and missing transverse momentum in $\sqrt{s} = 7 \text{ tev}$ proton-proton collisions. Technical Report arXiv:1110.6189. CERN-PH-EP-2011-165, CERN, Geneva, Oct 2011.
- [39] The ATLAS Collaboration. The atlas simulation infrastructure. 2010. cite arxiv:1005.4568 Comment: Submitted to Eur. Phys. J. C.
- [40] The CDF Collaboration. Observation of top quark production in $\bar{p}p$ collisions. 1995.
- [41] The D0 Collaboration. Combination of $t\bar{t}$ cross section measurements and constraints on the mass of the top quark and its decays into charged higgs bosons. *Phys. Rev. D*, 80:071102, Oct 2009.
- [42] G. Corcella et al. HERWIG 6.5: an event generator for Hadron Emission Reactions With Interfering Gluons (including supersymmetric processes). *JHEP*, 01:010, 2001.
- [43] G. Corcella et al. HERWIG 6.5 release note. 2002.
- [44] M J Costa. Commissioning of the atlas detector with cosmic rays and lhc beam data. Dec 2008. Discrete 08 starts December 11th.
- [45] D O Damazio. Atlas lar calorimeter: construction, integration and commissioning. *Journal of Physics: Conference Series*, 110(9):092007, 2008.
- [46] M. Ellert, M. Grønager, A. Konstantinov, B. Kónya, J. Lindemann, I. Livenson, J.L. Nielsen, M. Niinimäki, O. Smirnova, and A. Wäänänen. Advanced resource connector middleware for lightweight computational grids. *Future Generation Computer Systems*, 23(2):219 – 240, 2007.

- [47] Mattias Ellert, Michael Grønager, Aleksandr Konstantinov, Balázs Kónya, J. Lindemann, I. Livenson, Jakob Langgaard Nielsen, Marko Niinimäki, Oxana Smirnova, and Anders Wäänänen. Advanced resource connector middleware for lightweight computational grids. *Future Generation Comp. Syst.*, 23(2):219–240, 2007.
- [48] Alain Roy et. al. Building and testing a production quality grid software distribution for the open science grid. *Journal of Physics: Conference Series.*, 180(012052), 2009.
- [49] G.C. Blazey et al. Run II jet physics.
- [50] O. Smirnova F. Paganelli, Zs. Nagy. Arc computing element. Technical Report NORDUGRID-MANUAL-20, NorduGrid, 2011.
- [51] Ian T. Foster. Globus toolkit version 4: Software for service-oriented systems. *J. Comput. Sci. Technol.*, 21(4):513–520, 2006.
- [52] Ian T. Foster, Carl Kesselman, and Steven Tuecke. The anatomy of the grid - enabling scalable virtual organizations. *CoRR*, cs.AR/0103025, 2001.
- [53] Stefano Frixione, Paolo Nason, and Carlo Oleari. Matching NLO QCD computations with Parton Shower simulations: the POWHEG method. *JHEP*, 0711:070, 2007.
- [54] Stefano Frixione, Paolo Nason, and Giovanni Ridolfi. A Positive-weight next-to-leading-order Monte Carlo for heavy flavour hadroproduction. *JHEP*, 0709:126, 2007.
- [55] Patrick Fuhrmann and Volker Gülzow. dcache, storage system for the future. In Wolfgang E. Nagel, Wolfgang V. Walter, and Wolfgang Lehner, editors, *Euro-Par*, volume 4128 of *Lecture Notes in Computer Science*, pages 1106–1113. Springer, 2006.
- [56] M Hance, D Olivito, and H Williams. Performance studies for e/gamma calorimeter isolation. Technical Report ATL-COM-PHYS-2011-1186, CERN, Geneva, Sep 2011.
- [57] Michael Schmitt Jane Nachtman. The sliding q_t ratio method. Technical Report 7403, 2004.
- [58] Gordon L Kane. *Modern elementary particle physics the fundamental particles and forces*. Addison-Wesley, Reading, MA, 1993.

- [59] Jihn E. Kim and Gianpaolo Carosi. Axions and the strong cp problem. *Rev. Mod. Phys.*, 82:557–601, Mar 2010.
- [60] M. T. Grisaru L. Girardello. Soft breaking of supersymmetry. *Nucl. Phys.*, B194:65, 1982.
- [61] Paul Langacker. Z' physics at the LHC, 2009.
- [62] Volker Lindenstruth and Ivan Kisel. Overview of trigger systems. *Nuclear Instruments and Methods in Physics Research Section A: Accelerators, Spectrometers, Detectors and Associated Equipment*, 535(1-2):48 – 56, 2004. [|ce:title|Proceedings of the 10th International Vienna Conference on Instrumentation|/ce:title|](#).
- [63] Michelangelo L. Mangano, Mauro Moretti, Fulvio Piccinini, Roberto Pittau, and Antonio D. Polosa. ALPGEN, a generator for hard multiparton processes in hadronic collisions. *JHEP*, 07:001, 2003.
- [64] Stephen P. Martin. A Supersymmetry primer. 1997.
- [65] Paolo Nason. A New method for combining NLO QCD with shower Monte Carlo algorithms. *JHEP*, 0411:040, 2004.
- [66] B. Pontecorvo. Neutrino Experiments and the Problem of Conservation of Leptonic Charge. *Soviet Journal of Experimental and Theoretical Physics*, 26:984, May 1968.
- [67] J. Pumplin, D. R. Stump, J. Huston, H. L. Lai, P. Nadolsky, and W. K. Tung. New generation of parton distributions with uncertainties from global qcd analysis. 2002.
- [68] V. C. Rubin, W. K. J. Ford, and N. . Thonnard. Rotational properties of 21 SC galaxies with a large range of luminosities and radii, from NGC 4605 $R = 4\text{kpc}$ to UGC 2885 $R = 122\text{ kpc}$. *apj*, 238:471–487, June 1980.
- [69] Gavin P. Salam and Grégory Soyez. A practical seedless infrared-safe cone jet algorithm. *Journal of High Energy Physics*, 2007(05):086, 2007.
- [70] M Schulz. Data management for the lhc experiments: Requirements and challenges that drive the glite middleware development. page 149, 2010. 4th Iberian Grid Infrastructure Conference (IBERGRID), Braga, PORTUGAL, MAY 24-27, 2010.
- [71] Torbjörn Sjöstrand, Stephen Mrenna, and Peter Z. Skands. PYTHIA 6.4 Physics and Manual. *JHEP*, 05:026, 2006.

- [72] Daniel Stump et al. Inclusive jet production, parton distributions, and the search for new physics. *JHEP*, 10:046, 2003.
- [73] V. and Daniel Elvira. Jet measurements at d0 using a k_t algorithm. *Nuclear Physics B - Proceedings Supplements*, 121(0):21 – 28, 2003. Proceedings of the QCD 02 9th High-Energy Physics International Conference on Quantum ChromoDynamics.